Solar Physics (2024) 299:94
https://doi.org/10.1007/s11207-024-02337-4

RESEARCH

Decomposing the AIA 304 Å Channel into Its Cool and Hot Components

Patrick Antolin[1] · Frédéric Auchère[2] · Ethan Winch[3] · Elie Soubrié[2,4] · Ramón Oliver[4,5]

Received: 13 February 2024 / Accepted: 12 June 2024 / Published online: 2 July 2024

Abstract
The AIA 304 Å channel on board the *Solar Dynamics Observatory* (SDO) offers a unique view of $\approx 10^5$ K plasma emitting in the He II 304 Å line. However, when observing off-limb, the emission of the (small) cool structures in the solar atmosphere (such as spicules, coronal rain and prominence material) can be of the same order as the surrounding hot coronal emission from other spectral lines included in the 304 Å passband, particularly over active regions. In this paper, we investigate three methods based on temperature and morphology that are able to distinguish the cool and hot emission within the 304 Å passband. The methods are based on the Differential Emission Measure (DEM), a linear decomposition of the AIA response functions (RFit) and the Blind Source Separation (BSS) technique. All three methods are found to produce satisfactory results in both quiescent and flaring conditions, largely removing the diffuse corona and leading to images with cool material off-limb in sharp contrast with the background. We compare our results with co-aligned data from the *Interface Region Imaging Spectrograph* (IRIS) in the SJI 1400 Å and 2796 Å channels, and find the RFit method to best match the quantity and evolution of the cool material detected with IRIS. Some differences can appear due to plasma emitting in the $\log T = 5.1-5.5$ temperature range, particularly during the catastrophic cooling stage prior to rain appearance during flares. These methods are, in principle, applicable to any passband from any instrument suffering from similar cool and hot emission ambiguity, as long as there is good coverage of the high-temperature range.

Keywords Corona, structures · Heating, corona · Heating, in flares · Instrumental effects · Prominences · Spectral line, intensity and diagnostics · Spectrum, ultraviolet · Transition region

✉ P. Antolin
patrick.antolin@northumbria.ac.uk

1 Department of Mathematics, Physics and Electrical Engineering, Northumbria University, Newcastle upon Tyne, NE1 8ST, UK

2 Université Paris-Saclay, CNRS, Institut d'Astrophysique Spatiale, 91405, Orsay, France

3 Armagh Observatory and Planetarium, Armagh, Northern Ireland, BT61 7BH, UK

4 Institute of Applied Computing and Community Code, Universitat de les Illes Balears, E-07122 Palma de Mallorca, Spain

5 Departament de Física, Universitat de les Illes Balears, E-07122 Palma de Mallorca, Spain

1. Introduction

Temperature-determination techniques are essential in astrophysics. They are crucial in solar physics to advance in the solution of the coronal-heating problem. For this aim, data from spectrometers are by far the most reliable thanks to their narrower response function (Reale 2010; Cheung et al. 2019). However, the current absence of high-resolution fast scanning single-slit or multi-slit instruments in the corona has led us to often rely on narrowband ultraviolet (UV) or extreme ultraviolet (EUV) imagers. Despite being relatively narrow, such passbands typically include significant contributions from more than one ion, thus leading to uncertainty regarding the temperature of the observed plasma (Del Zanna and Mason 2018). In the coronal heating topic, this is particularly limiting for diagnosing very hot plasma, whose sole presence has been suggested as evidence for magnetic reconnection (Ishikawa et al. 2017; Hinode Review Team et al. 2019). For example, emission in the 94 passband of the *Atmospheric Imaging Assembly* (AIA: Lemen et al. 2012) on board the *Solar Dynamics Observatory* (SDO: Pesnell, Thompson, and Chamberlin 2012) is often interpreted as hot (7 MK), originating from Fe XVIII. However, the contribution of various lower ionised states of Fe within the passband can lead to low or medium temperatures dominating the emission, depending on the source region (Aschwanden and Boerner 2011; Testa et al. 2012). Warren, Winebarger, and Brooks (2012) and Del Zanna (2013) have provided a recipe based on AIA channel contribution for disentangling the hot Fe XVIII emission within the passband.

The AIA 304 Å channel is another perfect example of a passband in which emission from plasma at very disparate temperatures can mix. The temperature-response function peaks at $\approx 10^5$ K, due to He II 303.8 Å emission.

However, as shown in Figure 1, the passband also includes several other spectral lines, particularly Si XI 303.32 Å that peaks at $T \approx 2$ MK (Tousey et al. 1965), but also lines from O V (≈ 0.3 MK), Fe XVIII and Ca XVIII 302.19 Å (≈ 10 MK). Thompson and Brekke (2000) studied the relative intensity of He II and Si XI with the *Coronal Diagnostic Spectrometer* (CDS) aboard the *Solar and Heliospheric Observatory* (SOHO). They showed that, although an order of magnitude smaller on disk, when observing off-limb, the emission from Si XI dominates outside regions of cool plasma and can become comparable to the He II emission given the longer integration paths and the diffuse hot corona, which can be the case when observing spicules protruding off-limb, coronal rain or prominence material above active regions. In order to match measurements, We used an empirical factor of 5 to correct the He II intensities computed by CHIANTI (Dere et al. 1997; Del Zanna et al. 2021) to produce the response function of Figure 2. Disentangling the cool and hot components within passbands such as AIA 304 Å is particularly relevant for coronal heating. For example, heating to coronal temperatures in spicules is evidence that heating mechanisms already operate in these chromospheric structures (Rouppe van der Voort et al. 2015). The presence of coronal rain in the solar atmosphere is a strong proxy for strongly stratified, medium- to high-frequency heating in coronal structures (Antolin 2020) or even coronal-heating mechanisms (Antolin, Shibata, and Vissers 2010). Its precise quantity at any given time is therefore an important variable to determine (Şahin and Antolin 2022).

Several techniques have been developed that try to quantify the amount of plasma emitting in a given temperature range along a given line-of-sight (LOS). All of these rely on the availability of detailed atomic databases for multiple ions, such as CHIANTI (Dere et al. 1997; Landi et al. 2012), which allow us to construct temperature-response functions for instrument passbands. The availability of several passbands with temperature-response functions peaking at different temperatures simultaneously observing the Sun, notably from SDO/AIA, allows us to pose the problem of temperature determination, which is, however,

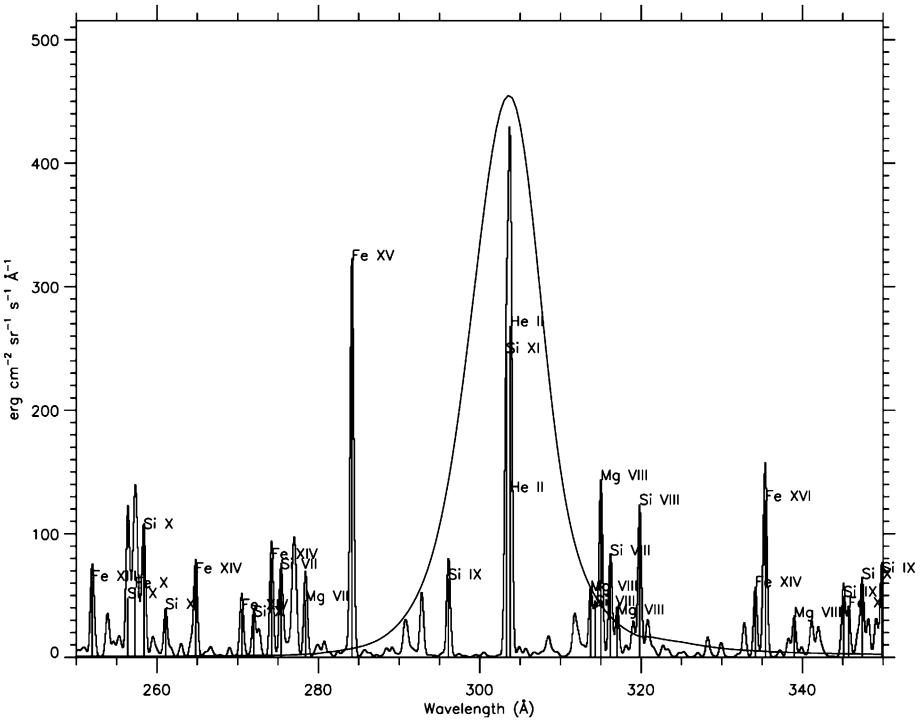

Figure 1 CHIANTI spectrum between 250 Å and 350 Å, along with the AIA spectral response function (in arbitrary units). Computed for a quiet-Sun DEM using Sun coronal 2021 abundances and CHIANTI default ionisation balance.

severely underconstrained. An example of this is the Differential Emission Measure (DEM: Jefferies, Orrall, and Zirker 1972; Jordan 1976), which links the temperature to the column mass along the LOS for an optically thin plasma. Schemes based on χ^2 minimisation (Kashyap and Drake 1998; Guennou et al. 2012; Hannah and Kontar 2012; Plowman and Caspi 2020) and sparsity (Cheung et al. 2015), and a combination with machine-learning algorithms (Wright et al. 2019) have been proposed to solve the DEM inversion. Loboda et al. (2023) used the DEM method in a first attempt to disentangle the He II and Si XI emission included in the AIA 304 Å passband in quiet-Sun and coronal-hole regions. Based on the relatively constant temperature variation with height in the corona and the approximatively plane-parallel atmosphere characteristic of those regions, they estimate the emission measure and density variation with height, from which the Si XI emission is inferred. Precise knowledge of the temperature-response functions of each passband can also significantly help (and is essential in the DEM inversion) in quantifying the multi-thermal emission. Warren, Winebarger, and Brooks (2012) and Del Zanna (2013) have used the shape of the AIA 171 Å and AIA 193 Å response functions to estimate the cool emission in the AIA 94 Å channel, thereby identifying better the hot Fe XVIII emission within the passband.

Another temperature-determination method is the Blind Source Separation (BSS), through which an image is decomposed into a number of sources that are morphologically independent of each other (Common and Jutten 2010; Kuruoglu 2010). When applied to the solar corona, for which distinct morphological features appear in different EUV passbands (Cheng, Smith, and Tandberg-Hanssen 1980; Gallagher et al. 1998; Feldman, Widing, and

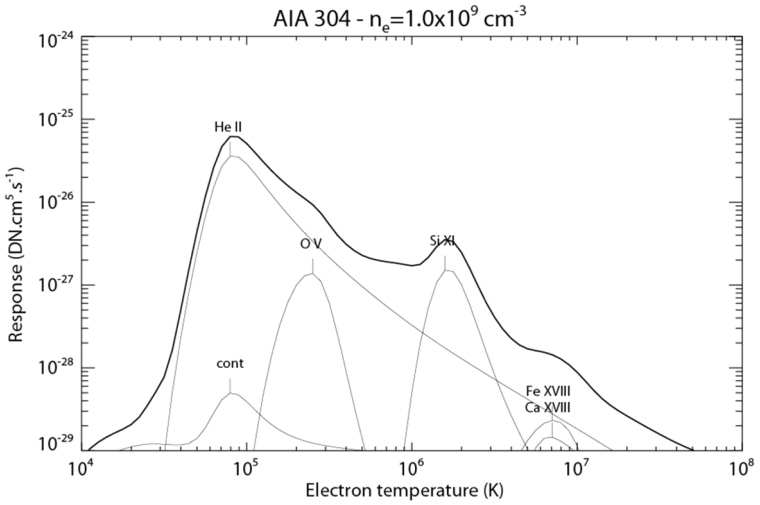

Figure 2 Response function of the AIA 304 Å passband along with the contribution functions of the individual ions that cause the main features in the total response. Computations are made at a constant density of 10^9 cm^{-3}. An empirical factor 5 was included for the 304 Å line of He II.

Warren 1999), the independent sources are identified with narrower temperature responses from which more thermally pure images can be obtained (Dudok de Wit and Auchère 2007; Dudok de Wit et al. 2013).

By quantifying the amount of hot plasma in a given passband it is therefore possible to infer the amount of cool emission, even when such emission is optically thick, as is the case for AIA 304 Å. In this paper, we explore the decomposition of this passband into hot and cool components by using the DEM and BSS methods, and the RFit method. In Section 2 we introduce the observations and in Section 3 we present the methods. The results are presented in Section 4 and discussed in Section 5.

2. Observations

For the purpose of testing the methods we focus on a specific dataset obtained with the *Atmospheric Imaging Assembly* (AIA: Lemen et al. 2012) on board the *Solar Dynamics Observatory* (SDO: Pesnell, Thompson, and Chamberlin 2012) and the *Interface Region Imaging Spectrograph* (IRIS: De Pontieu et al. 2014) of an active region (AR) off-limb, observed on 13 March 2014. We select this dataset early in both missions to reduce the impact of instrumental degradation. The co-observation runs from 13 March 2014 23:34:46UT to 14 March 2014 01:22:58UT.[1] Level-2 images were used for both SDO/AIA and IRIS. The level-2 AIA data corresponds to 1.5-level data further calibrated by Lockheed Martin Solar and Astrophysics Laboratory (LMSAL) to include initial co-alignment with IRIS) (taking into account roll angle) with a field-of-view (FOV) of $397'' \times 406''$ centred at $(x, y) = (971'', 304'')$. The AIA data has a temporal resolution of 12 s for the EUV channels and a plate scale of $0.6'' \times 0.6''$. The IRIS observation program for this dataset corresponds to an IHOP 248 program (coordinated with Hinode), with OBSID 3840259454 that consisted of a very large

[1]The level-2 datasets for both instruments can be found here.

Table 1 Instrument and passbands used in this study. The 'EUV' label under Passband for AIA denotes all the EUV channels of AIA (094 Å, 131 Å, 171 Å, 193 Å, 211 Å, 304 Å, 335 Å). The plate scale specifies only one spatial dimension, with the other dimension being the same. The exposure time for AIA varies according to the passband, with values within the specified range. Δt in the last column denotes the duration of the datasets, with the AIA and IRIS datasets starting at 23:24:43UT and 23:34:46UT on the 13 March 2014, respectively. For further information see Section 2.

Instrument	Passband	Plate scale [arcsec]	Cadence [s]	Exp.time [s]	FOV [arcsec^2]	Δt [min]
SDO/AIA	EUV	0.6	12	2 – 2.9	397 × 406	127.8
IRIS/SJI	1400 Å, 2796 Å	0.166	18.5	8	167 × 175	107.8

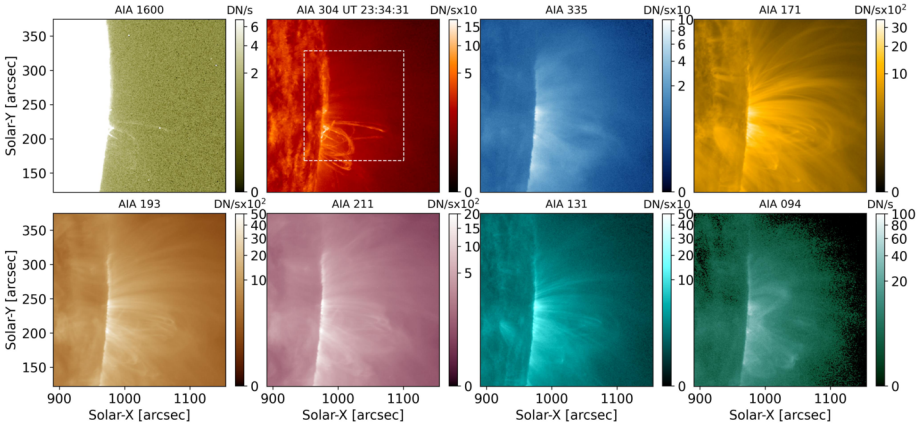

Figure 3 A snapshot in various SDO/AIA channels closest in time to 13 March 2014 23:34:46UT focusing on an AR at the West limb of the Sun. The channels are ordered with respect to increasing temperature from left to right and top to bottom, taking the peak formation temperature of the dominating ion. The dashed white square within the AIA 304 Å FOV corresponds to the IRIS FOV, shown in Figure 5. The AIA 1600 Å channel has been saturated in order to show the quiescent coronal rain. The intensities have been scaled as a power law with 0.3 index in order to reduce the dynamic range present in the original data and better see the structure.

sit-and-stare (FOV of 167″ × 175″ co-centred with the AIA FOV) with a small line list and included SJI 1400 Å and 2796 Å. The FOV has the same centre as that of the AIA cutouts and has a 20° roll angle that leads to a slit parallel to the limb. In this work, we will use both SJI data, which have a cadence of 18.5 s, an exposure time of 8 s and a plate scale of 0.166″ × 0.166″. Table 1 summarises the main information of the datasets used in this work.

Another reason behind the choice of this dataset is the presence of an M1.2 flare during the observation sequence. The flare is observed to occur in the top half of the FOV, starting on 13 March 2014 at 23:45UT (20 min after the start of the observation sequence), reaching a peak on 14 March 2014 at ≈ 00:10UT, and with the flare-driven rain appearing at 00:55UT. The strong morphology and temperature variation observed during flares constitute a great test bed for the presented methods. In Figures 3 and 4 we show, respectively, the AR at the beginning (13 March 2014 23:34:46UT) and towards the end (14 March 2014 01:14:43UT) of the observation, with the latter showing clearly the flare loop in the gradual phase of the flare. We will refer to these initial and later stages of the AR as 'quiescent' and 'flaring', respectively. In Figure 5 we show the corresponding IRIS images, closest in time to those shown in the previous figures.

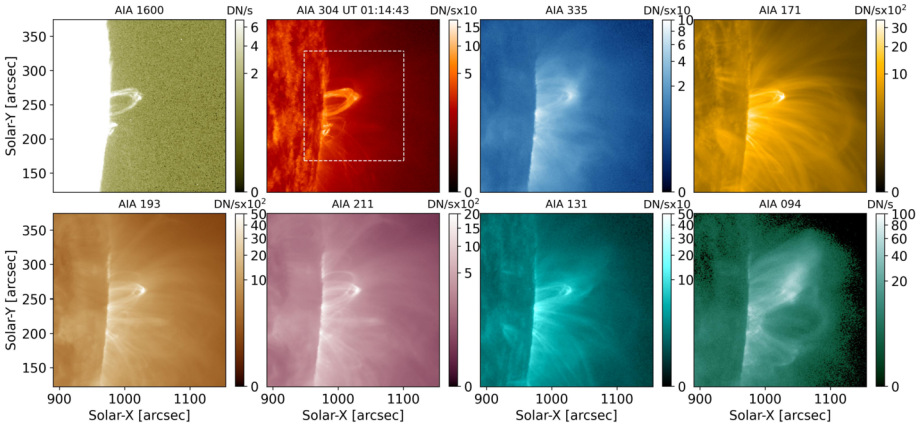

Figure 4 Same as in Figure 3 but for 14 March 2014 01:22:58UT during an M1.2 flare.

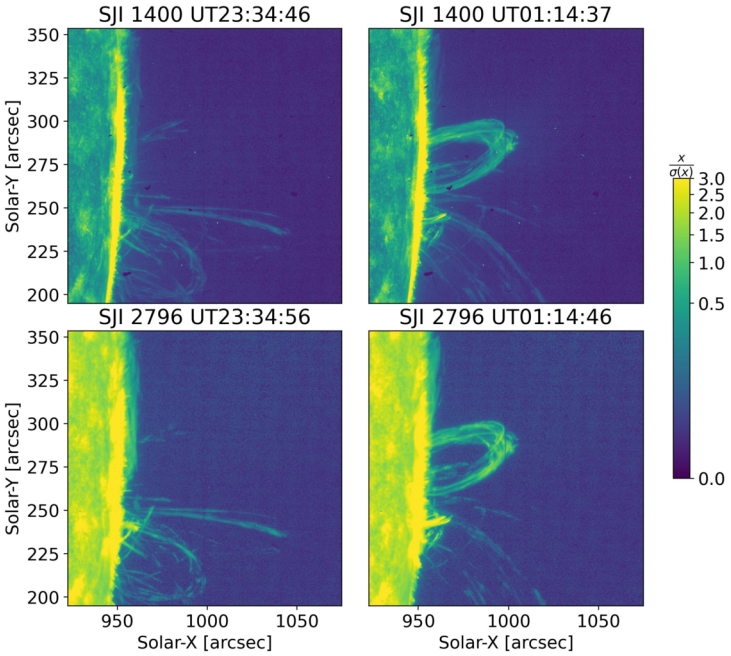

Figure 5 The IRIS FOV on 13 March 2014 23:34:46UT (left) and 14 March 2014 01:14:37UT (right) in the SJI 1400 Å (top) and SJI 2796 Å (bottom) channels. This FOV is contained within the AIA FOV shown in Figures 3 and 4. Each image has been normalised by its standard deviation and the resulting values have been scaled as a power law with 0.3 index in order to better see the structure.

3. Methodology

The AIA 304 Å response function is dominated by He II emission at 303.8 Å (see Figure 2), which has a maximum temperature formation of $\log T \approx 4.8$. However, the passband also includes a significant secondary component produced by Si XI emission at 303.32 Å, with a

temperature formation of $\log T \approx 6.2$. Due to the very different temperatures, we will refer to these as the cool and hot components of the AIA 304 Å passband. As seen in Figure 2, the peak of the AIA 304 Å response function at 10^5 K is more than one order of magnitude larger than the peak at $\approx 1.5 \times 10^6$ K. However, the optically thin corona and long line-of-sight (LOS) integration paths compared to the thin transition-region plasma can often compensate this difference in the response function and lead to comparable intensities in AIA 304 Å images. This is particularly the case for off-limb observations of active regions, for which the LOS integration paths are longest, and that often host coronal rain at $10^4 - 10^{5.5}$ K temperatures[2] in addition to the hot multi-million coronal environment. Similar intensity values can be seen in quiescent conditions, as shown in Figure 3. The cool component can be seen as clumpy in AIA 304 Å images, due to the clumpy and compact morphology of the rain, while the hot component appears diffuse. While the intensities of both components can be comparable their morphologies can appear completely different.

There are therefore two major avenues for distinguishing the cool and hot components of a AIA 304 Å image. The first and foremost is based on temperature. If we know the temperature of the plasma then we can easily disentangle the emission. Temperature derivation can be made with the knowledge of the AIA response functions and we highlight two methods: an AIA 304 Å response fitting method (RFit) and the Differential Emission Measure (DEM) method. The second avenue is entirely based on morphology, and makes use of the Blind Source Separation (BSS) technique. For all the following techniques we normalise the AIA images with respect to the exposure time. This is particularly important for the RFit and DEM methods, for which the response function values are per unit time. We also normalise the IRIS images with respect to exposure time for better comparison with the AIA images.

It is important to note that CHIANTI fails at reproducing the intensity peak of the He II emission at $10^{4.8}$ K, giving an order of magnitude lower values. This discrepancy was initially attributed to photoionisation by coronal radiation (Zirin 1988), which was later rebuked by Andretta, Del Zanna, and Jordan (2003), favouring instead collisional excitation in a process termed velocity redistribution (Jordan 1980) for the expected large turbulence motions mixing hot and cold plasma in the TR (see Andretta, Del Zanna, and Jordan 2003, for more detail). More recently, Golding, Leenaarts, and Carlsson (2017) have shown that the effects of non-equilibrium ionisation combined with optically thick radiative transfer can account for the large intensities of the He II line. To properly model the response function of AIA, the obtained response function from CHIANTI is multiplied by an empirical factor of 5 (also applied in Figure 2), proposed by O'Dwyer et al. (2010) based on the values measured by Vernazza and Reeves (1978). This empirical approach has little effect on the tested methods. The DEM is not affected because He II is not used in the inversion. The BSS is based on morphology and does not know anything about the passband content. Finally, as we will see in the following section, the RFit method only models the hotter component of AIA 304 Å and is therefore not affected by the empirical He II factor.

The repository for the following three methods can be found at Antolin (2024).

3.1. Response Fit (RFit) Method

This method is based on the knowledge of the AIA 304 Å response function with respect to temperature. For the present work we take the response function from Solarsoft, obtained with the command `aia_get_response(/dn,/temp,/chiantifix,/eve,`

[2]These extremum values are approximate. Coronal rain at lower or higher temperatures is possible (Antolin et al. 2015).

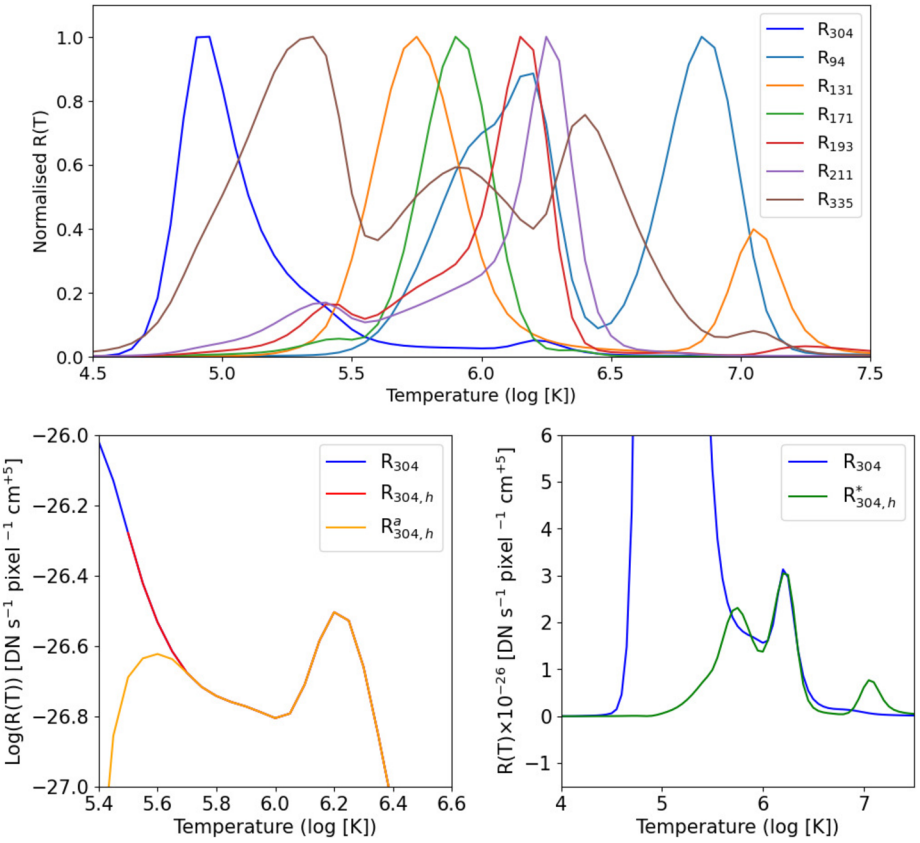

Figure 6 Top: Normalised AIA EUV response functions (including AIA 304 Å) with respect to temperature for 13 March 2014. Bottom left: Apodised AIA 304 Å response function over the high-temperature range ($R^a_{304,h}$) used to generate $R^*_{304,h}$ in the bottom right panel. The function $R_{304,h}$ is used for the DEM method and is equal to R_{304} in the range $\log T > 5.5$ and is 0 otherwise. Bottom right: $R^*_{304,h}$ is the fitting result of $R^a_{304,h}$ using the remaining 6 EUV channels, used in the RFit method.

`timedepend_date=date)` where `date='2014-03-13T23:24:43.120'` corresponds to a time near the start of the selected dataset in this study. In this command, the '`dn`' keyword means DN units, the '`temp`' keyword specifies the temperature-response function, the '`chiantifix`' keyword applies an empirical correction to the AIA 94, and AIA 131, channels to account for emission not included in CHIANTI (Aschwanden and Boerner 2011), and the '`eve`' keyword provides good overall agreement with the Extreme Ultraviolet Variability Experiment (EVE) of SDO. The normalised response functions for the 6 EUV channels and AIA 304 Å are shown in Figure 6 (top panel). Solarsoft calculates this response function with the help of the CHIANTI atomic database (Dere et al. 1997; Landi et al. 2012). In this work, we use CHIANTI version 10 (Del Zanna et al. 2021). However, it is important to note that the emissivity tables of this CHIANTI version are the same as those of version 9. By default, the AIA command above includes an empirical factor of 5 multiplying the 304 Å response function, which has also been applied in Figure 2. We can see that the cool peak of the AIA 304 Å passband is isolated on the left-hand side of the temperature range, but the secondary hot peak is well covered by the other EUV response

functions of AIA. This means that we can always find a suitable linear decomposition of the hot part of the AIA 304 Å response function in terms of all the other EUV response functions. To this end, we first define everything above $\log T = 5.75$ as being part of the 'hot' AIA 304 Å emission. We set everything below $\log T = 5.32$ to 0 and apodise with a sine function between the values of $\log T = 5.32$ and $\log T = 5.75$ to obtain $R^a_{304,h}$, the hot AIA 304 Å response function to fit, shown in the bottom left panel of Figure 6, according to Equation 1:

$$R^a_{304,h} = \begin{cases} R_{304,h}, & \text{if } \log T > 5.75 \\ \frac{1}{2}\left(1 + \sin(\frac{\log T - 5.535}{0.43}\pi)\right) R_{304,h}, & \text{if } 5.32 < \log T < 5.75 \\ 0, & \text{if } \log T < 5.32. \end{cases} \tag{1}$$

The apodisation reduces effects from fitting the lower temperature boundary. With a least-squares method, we then minimise the fit to $R^a_{304,h}$ with all the other response functions, obtaining $R^*_{304,h}$:

$$\begin{aligned} R^*_{304,h} &= c_{94}R_{94} + c_{131}R_{131} + c_{171}R_{171} + c_{193}R_{193} + c_{211}R_{211} + c_{335}R_{335}, \\ \Rightarrow R^*_{304,h} &= \sum_i c_i R_i, \end{aligned} \tag{2}$$

where the c_i denote the coefficients $c_{94}, \ldots, c_{335}$ resulting from the fitting, and the R_i denote the respective response functions.

Note that the range of the apodisation will influence the shape of $R^*_{304,h}$ and some fine tuning is required in order to make it as close as possible to R_{304}. Since this method is based on the response functions and these change over time due to instrumental degradation, the best results are obtained when using response functions close in time to any particular AIA data of interest. The result of the fitting process for the particular AIA 304 Å response function shown in Figure 6 is depicted in the bottom right panel, for which the coefficients are $c_{94} = -0.01656702$, $c_{131} = 0.06593333$, $c_{171} = -0.00041376$, $c_{193} = 0.0026049$, $c_{211} = 0.01227751$, $c_{335} = -0.00096265$. Note that in this particular decomposition, some response functions contribute minimally (171 Å, 193 Å and 335 Å), and similar results can be obtained with a subset. We have experimented with various subsets of channels, as well as different boundaries for the 'hot' temperature range in the AIA 304 Å passband, and found very similar results, with no combination or apodisation being significantly better.

Equation 2 provides an approximation to the hot component of the 304 Å intensity $I_{304,h}$ with the other EUV intensities, thereby obtaining $I^{\mathrm{RFit}}_{304,h}$, where 'RFit' denotes this response fit method:

$$\begin{aligned} R^*_{304,h} &= \sum_i c_i R_i \\ \Rightarrow \int DEM(T) R^*_{304,h} dT &= \int DEM(T) \sum_i c_i R_i dT \\ \Rightarrow \int DEM(T) R^*_{304,h} dT &= \sum_i \int c_i DEM(T) R_i dT \\ \Rightarrow I^{\mathrm{RFit}}_{304,h} &= \sum_i c_i I_i = \mathbf{c} \cdot \mathbf{I}, \end{aligned} \tag{3}$$

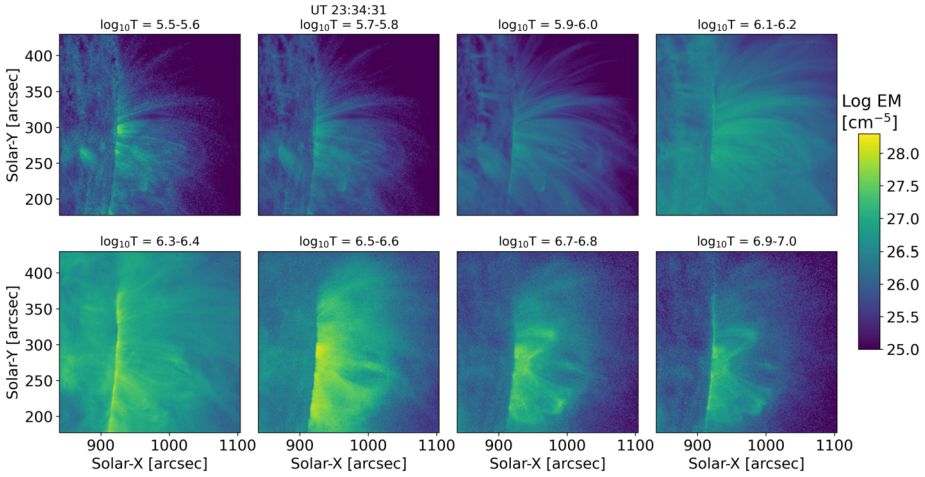

Figure 7 The emission measure maps (on a logarithmic scale) at specific temperature bins obtained from the simple regularisation method by Plowman and Caspi (2020) for the current dataset at the quiescent active-region time (same time as in Figure 3).

where the I_i correspond to the respective intensities from the other 6 AIA channels. To obtain the cool component of the AIA 304 Å image, $I^{\mathrm{RFit}}_{304,c}$, we then simply subtract the hot component from the original image I_{304}:

$$I^{\mathrm{RFit}}_{304,c} = I_{304} - I^{\mathrm{RFit}}_{304,h}. \tag{4}$$

3.2. DEM-Based Method

The Differential Emission Measure (DEM) method provides the amount of optically thin plasma along the LOS emitting in specific temperature bins. Hence, by convolving the emission with the hot AIA 304 Å response function we obtain the amount of plasma that contributes to the hot component. For the DEM calculation we use the simple regularisation method by Plowman and Caspi (2020), available in SolarSoft as `'simple_reg_dem.pro'`, with the same 6 EUV channels as with the RFit method, and define 17 temperature bins from $\log T = 5.5$ to $\log T = 7.1$ with a 0.1 temperature step in log space, that is, the temperature for each bin is $\log T_{bin,\,j} = 5.5 + 0.1\,j$, with $j = 0, \ldots, 16$. The resulting DEM maps in selected temperature bins are shown in Figures 7 and 8 for, respectively, the quiescent and flaring stages of the AR. Note that very high temperature loops exist also during the quiescent time. We have checked that the average χ^2 values of the DEM results over the temperature-bin maps are reasonable, with only a few pixels above 1.5 (and usually corresponding to very far pixels from the limb).

The hot AIA 304 Å image obtained with the DEM method is then:

$$\begin{aligned} I_{304,h} &= \int DEM(T) R_{304,h} dT \\ &= \sum_{j=0}^{16} EM_j(T_{\mathrm{bin},\,j}) R_{304,h}(T_{\mathrm{bin},\,j}) \\ \Rightarrow I^{\mathrm{DEM}}_{304,h} &= EM(T_{\mathrm{bin}})^{\mathsf{T}} \cdot R_{304,h}(T_{\mathrm{bin}}), \end{aligned} \tag{5}$$

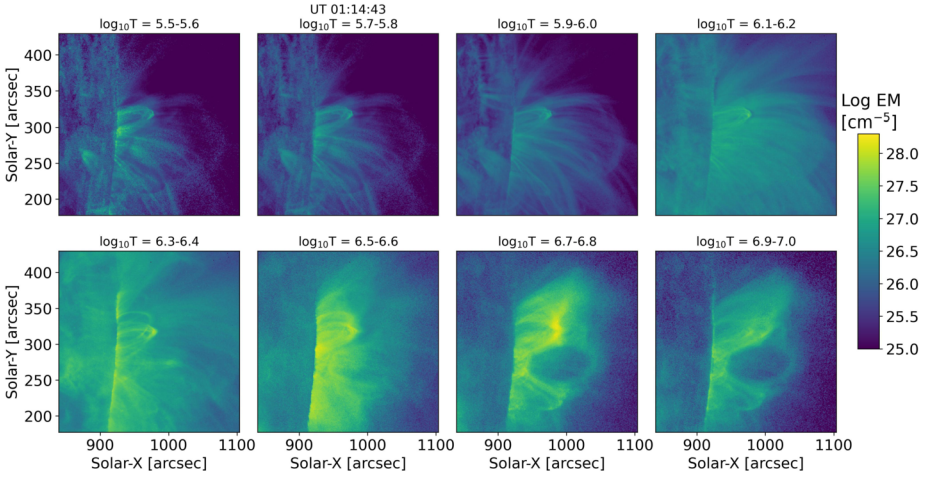

Figure 8 Same as in Figure 7 but for the flaring time (same as in Figure 4).

where $R_{304,h}(T_{\rm bin})$ is the non-apodised 304 Å response function shown in red in Figure 6 (bottom left panel) that only includes the range $\log T > 5.5$ and is evaluated at the 17 temperature values (bins) of the DEM. The $EM(T_{\rm bin})^{\rm T}$ is the transpose of the emission measure vector over all temperature bins.

This DEM-based method therefore provides the cool AIA 304 Å image by removing the hot component from the original image:

$$I^{\rm DEM}_{304,c} = I_{304} - I^{\rm DEM}_{304,h}. \tag{6}$$

3.3. BSS Method

The method of Blind Source Separation (BSS) assumes that a signal or image can be decomposed into sources that are independent of each other, using the least amount of prior information (Nuzillard and Bijaoui 2000; Delabrouille, Cardoso, and Patanchon 2003; Common and Jutten 2010; Kuruoglu 2010). For the current problem, given an image in an AIA passband λ, I_λ, we would have:

$$I_\lambda = \sum_{k=1}^{N} V_{k,\lambda} S_k + B_\lambda, \tag{7}$$

where S_k are the source components, $V_{k,\lambda}$ are called mixing coefficients and B_λ is an error term that incorporates model uncertainties as well as instrumental noise and other errors. We then have a set of m equations, one for each AIA passband. The source terms and mixing coefficients are then obtained by minimising the errors. However, as in the DEM method (see Section 3.2), this is a very ill-posed problem and several assumptions are usually taken when looking for a particular solution (such as positivity and mutual independence). The DEM equation actually has the same shape as Equation 7, as can be seen in Cheung et al. (2015). In Equation 7, the number N in the sum denotes the number of sources, and is another parameter that must be specified in advance. In the context of solar physics, the BSS framework has been applied in imaging with EIT (Dudok de Wit and Auchère 2007) or AIA

EUV images (Dudok de Wit et al. 2013), based on the fact that various passbands that cover different parts of the EUV spectrum are highly correlated because of the overlap in terms of their temperature sensitivity, as evidenced by Figure 6 (top panel). The aim is therefore to identify a minimum number N of source images with which we can recover most of the original image in each passband. The separation is solely based on morphological differences, which are indirectly linked to the temperature. This is particularly interesting for our case, since the cool and hot components of the 304 Å channel have, a priori, very different morphologies.

Several techniques have been used to recover the sources and mixing coefficients. Dudok de Wit and Auchère (2007) used The Singular Value Decomposition (SVD) and Independent Component Analysis (ICA) and found the latter to be more effective. Dudok de Wit et al. (2013) used the Bayesian Positive Source Separation (BPSS: Moussaoui et al. 2006) technique, which enforced the positivity of the sources. It is based on Bayesian estimation theory and uses a Markov Chain Monte Carlo method, which significantly increases the computation time. Here, we will use the fixed-point fast Independent Component Analysis (FastICA) method (Hyvarinen 1999), which works on minimising mutual information and deriving projection pursuit directions. The particular version of FastICA used is that provided by the `scikit-learn` python package, based on Hyvärinen and Oja (2000). FastICA has the advantage of being robust and offers a significant increase in speed. Dudok de Wit et al. (2013) have solved Equation 7 with $N = 3$, $N = 4$ and $N = 5$ terms, and noticed that for $N > 3$ not much improvement is obtained. Hence, we have considered $N = 2$ and $N = 3$, and found that $N = 2$ is not only sufficient but provides better results than with $N = 3$. Given the large overlap between passbands, it is also not necessary to take all EUV images when solving Equation 7. We have tested with various combinations and obtained satisfactory results with I_{304}, I_{193}, I_{211}, and I_{335}.

As shown by Dudok de Wit et al. (2013), each source function concentrates on a specific class of morphological structures and is best correlated with specific response functions. In essence, this can indirectly make the sources better temperature gauges. For our problem we have:

$$\begin{aligned} I_{304} &= \sum_{k=1}^{2} V_{k,304} S_k, \\ &= V_{c,304} S_c + V_{h,304} S_h \\ &= I^{\mathrm{BSS}}_{304,c} + I^{\mathrm{BSS}}_{304,h}, \end{aligned} \tag{8}$$

where I_{304} is the original 304 Å image, $V_{k,304}$ and S_k are, respectively, the mixing coefficients and source terms obtained from the chosen BSS method (FastICA algorithm in our case), with $k = c$ denoting the cool component and $k = h$ denoting the hot component. Thus, $I^{\mathrm{BSS}}_{304,c} = V_{c,304} S_c$ is the cool 304 Å component of the AIA image, and $I^{\mathrm{BSS}}_{304,h} = V_{h,304} S_h$ is the corresponding hot 304 Å component.

Prior to the minimisation with FastICA, each image must be pre-whitened, or centred (by subtracting the average so that the expectancy of each pixel is 0) and whitened (dividing by the standard deviation so that the variance is 1). An unwelcomed consequence of this is that the output data is no longer in physical units, and it is not possible to reverse the whitening steps. Hence, this method is more limited than the RFit and DEM methods.

The difference between the cool and hot 304 Å components in terms of morphology guarantees that $I^{\mathrm{BSS}}_{304,c}$ and $I^{\mathrm{BSS}}_{304,h}$ will be strongly correlated with the cool and hot 304 Å components, respectively. Along this line of thought, caution must be taken since in theory it is possible to have cool and hot plasma with opposite morphologies to those usually observed.

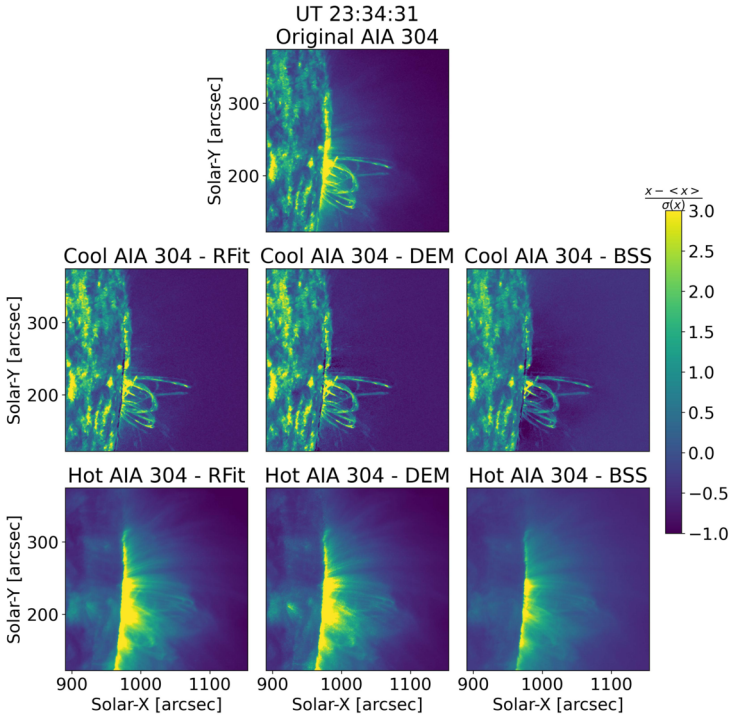

Figure 9 Comparison between the methods for the quiescent stage. The top image shows the original AIA 304 Å at 23:34:31UT, towards the beginning of the time sequence (quiescent stage). The middle row shows the cool 304 Å components corresponding to the original AIA 304 Å image, i.e. from left to right, $I^{\mathrm{RFit}}_{304,c}$, $I^{\mathrm{DEM}}_{304,c}$ and $I^{\mathrm{BSS}}_{304,c}$. The bottom row shows the respective hot 304 Å components for the AIA 304 Å image (in the same order), $I^{\mathrm{RFit}}_{304,h}$, $I^{\mathrm{DEM}}_{304,h}$, and $I^{\mathrm{BSS}}_{304,h}$. Note that the images have been whitened (see text for details) to allow better comparison. See accompanying animation.

4. Results

4.1. Comparison Between the Methods

In Figures 9 and 10 we show the results of the Response fit ('RFit'), DEM-based and BSS methods for the quiescent and flaring stages of the AR, respectively. In addition to the cool AIA 304 Å images, we also show the hot AIA 304 Å components for all methods. Since the BSS image has been pre-whitened, we also whiten all the other images (obtained with RFit and DEM) to allow comparison. That is, we show $(X - < X >)/\sigma(X)$, where $< X >$ and $\sigma(X)$ denote the average and standard deviation over the given image X, respectively.

The cool AIA 304 Å images can be seen to show far less diffuse emission off-limb, providing higher contrast for cool material such as coronal rain or spicules. The cool RFit and DEM solutions are very similar, with a very homogeneous off-limb background in which very faint rain clumps can be seen. On the other hand, the cool BSS solution has a more strongly varying background with negative values close to the limb. The rain-clump values also appear dimmer (and more uniform) than with the other methods. Some quiet on-disc regions also seem to be in sharper contrast in all the cool 304 Å images compared to the original image. All methods identify a thin layer of hot emission at the footpoints of many

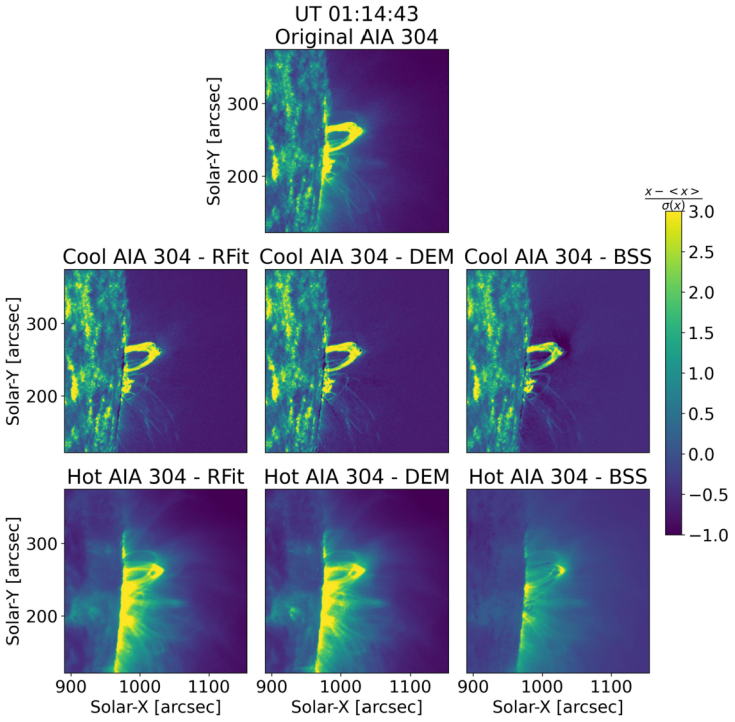

Figure 10 Comparison between the methods for the flaring stage. Same order as in Figure 9 for a time during the gradual phase of the flare (UT 01:14:43).

active-region loops. This enhanced hot emission may be due to the longer LOS and higher density of hot structures near the limb. As expected, the limb appears bright in the hot AIA 304 Å image. Some differences appear across the hot 304 Å images. However, these are likely due to the different standard deviation by which each image is normalised. Overall, the hot 304 Å component images look similar to the DEM results between $\log T = 5.5$ and 6.2, matching the range of the response function over which the hot 304 Å component is defined.

Similar results are obtained during the gradual phase of the flare. As seen in Figure 10, in this case very hot emission can become strongly localised at the loop top, and all three methods seem successful in the decomposition. This is particularly surprising for the BSS method, which solely works based on morphology. The RFit and DEM methods lead to stronger hot emission near the footpoints, but this is likely due to the difference in the normalisation produced by the whitening process. As a result, the hot loops are better seen in the BSS solution due to the lower range in values. However, as we will see in more detail in Section 4.2, all methods fail at properly decomposing the cool and hot components around the peak of the flare. As seen in the animation of Figure 9, the flare loop is significantly brighter in the hot RFit image, followed by the DEM image and is barely seen in the hot BSS image. This is inversely reflected in the cool 304 Å versions, with cool BSS showing the brightest emission, followed by DEM and then RFit during this time.

To more quantitatively understand the results we show in Figure 11 the percentage absolute difference between the original AIA 304 Å image and the respective cool AIA 304 Å

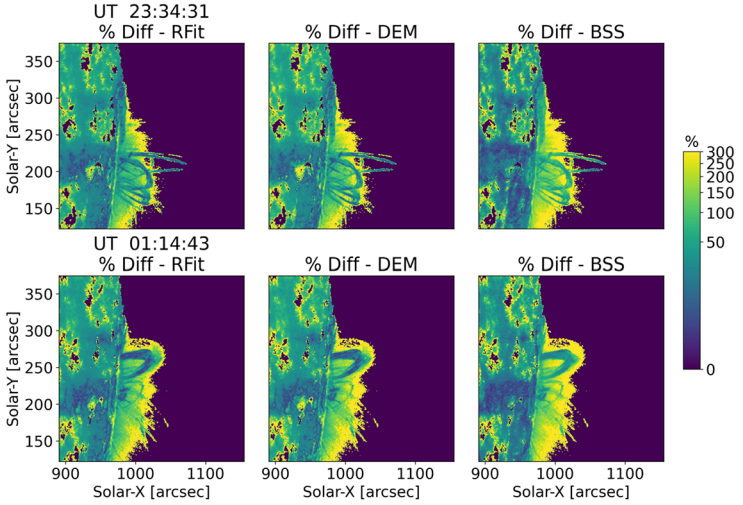

Figure 11 Images showing the percentage difference as defined in Equation 9 for the quiescent (top) and flaring (bottom) stages, for the RFit (left), DEM (middle) and BSS (right) methods. Note that the colour is plotted on a logarithmic scale.

image for each method, defined as:

$$\mathrm{Diff}_X = \frac{|\bar{I}_{304} - \bar{I}^X_{304,c}|}{\bar{I}_{304}}, \tag{9}$$

where $\bar{I}^X_{304,c}$ denotes the whitened cool AIA 304 Å component obtained with method $X =$ RFit, DEM or BSS. We limit this calculation to the pixels where the whitened $\bar{I}_{304}$ values are above 0. This essentially ignores the pixels with very small values at the noise level far from the limb, allowing to better appreciate the differences on the cool but dim structures off-limb.

As expected, we note that the biggest changes ($> 100\%$) occur for the off-limb cool structures and around them. Around the AR off-limb, excepting the loops with rain, the differences are significant ($100-200\%$), as expected from the large diffuse hot emission in the AR. The differences gradually increase with height due to the very low intensity values. As each image is normalised by its own standard deviation (and in the BSS case, the division by the standard deviation is done prior to the FastICA application) it is only possible to compare the general trends between the percentage difference images.

In Figure 12 we plot for each intensity value (in DN s^{-1}) of the original 304 Å image, the average percentage difference for the corresponding pixels in the cool AIA images over all images in the observational sequence (including quiescent and flaring regimes), with the error bars indicating the standard deviation in time. Here, we clearly see that the low off-limb intensities are those with highest percentage difference. A similar amount and trend in the scatter is observed across all methods, with the largest scatter observed for pixel intensities around $50-100$ DN s^{-1}, which correspond to the bright region around the limb. This is likely due to the stronger LOS superposition close to the limb, with the expected strong mix of cool and hot structures at low heights. We note larger standard deviations throughout most of the intensity range for the BSS method, which is likely due to the whitening process

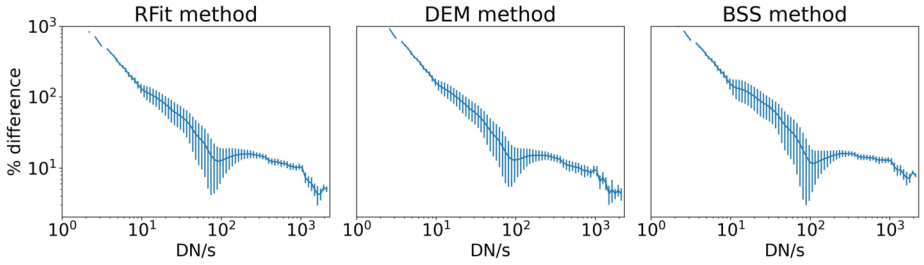

Figure 12 Intensity (in DN s^{-1}) versus percentage difference. The range of intensity values corresponds to the original AIA 304 Å images and is divided into 100 bins. Each bin therefore represents a group of pixels in the image sequence, and we calculate the average and standard deviation of the percentage difference for those pixels in the cool AIA images in each method (according to Equation 9) over all snapshots in the observational sequence (including quiescent and flaring stages).

(each image has a different standard deviation and mean, which introduces more variability in the cool–hot decomposition.)

Regarding the BSS method, we have tried a source number of $N = 2$ and $N = 3$, and found similar results, with a slight improvement with $N = 2$ in the sense that lower image-to-image variation is obtained (i.e. increased robustness). This suggests that the morphological difference between cool and hot plasmas in the solar atmosphere dominates over that existing between hot plasmas (e.g. warm versus hot or hot versus flaring plasma structures). For the $N = 3$ case, two components always correspond to 'hot' sources, and suggests the existence of two populations of hot loops. Moreover, one of the two hot sources is similar to the AIA 94 Å image, suggesting that the emission from Ca XVIII 302.19 Å dominates one of the two hot sources. However, a proper investigation of this hot versus flaring disambiguation with AIA 304 Å warrants a separate study.

4.2. IRIS–AIA Comparison

To test the ability to capture faint, off-limb cool material such as coronal rain it is further interesting to compare with higher-resolution IRIS observations in the SJI 1400 Å passband, which is dominated by Si IV 1402.77 Å emission and has a maximum temperature formation of $10^{4.8}$ K, that is, very similar temperature to that of the cool 304 Å component. We also compare with IRIS observations in the SJI 2796 Å passband, which is dominated by Mg II 2796.35 Å emission that has a maximum temperature formation of 10^4 K. This comparison provides a way to more properly differentiate the 304 Å emission obtained in each method.

When comparing results it is important to have in mind that IRIS has ≈ 1.8 times higher spatial resolution than AIA, so that structures such as rain clumps appear smaller in the SJI passbands. Furthermore, the two lines have very different opacities, with the He II line often becoming optically thick for chromospheric material, unlike the Si IV line. Moreover, the He II line is strongly affected by non-equilibrium ionisation (Golding, Leenaarts, and Carlsson 2017), often leading to stronger intensities than the optically thin values, which can be different for Mg II or Si IV (Leenaarts et al. 2013; Olluri et al. 2015).

In Figures 13 and 14 we show the co-observed region in the quiescent stage in SJI 1400, SJI 2796, the original AIA 304 Å and the cool and hot AIA 304 Å images obtained with the three methods. In Figure 13 we plot the images on a logarithmic scale such that the noise levels and the faintest cool pixels can be seen. We here retain the physical units where possible

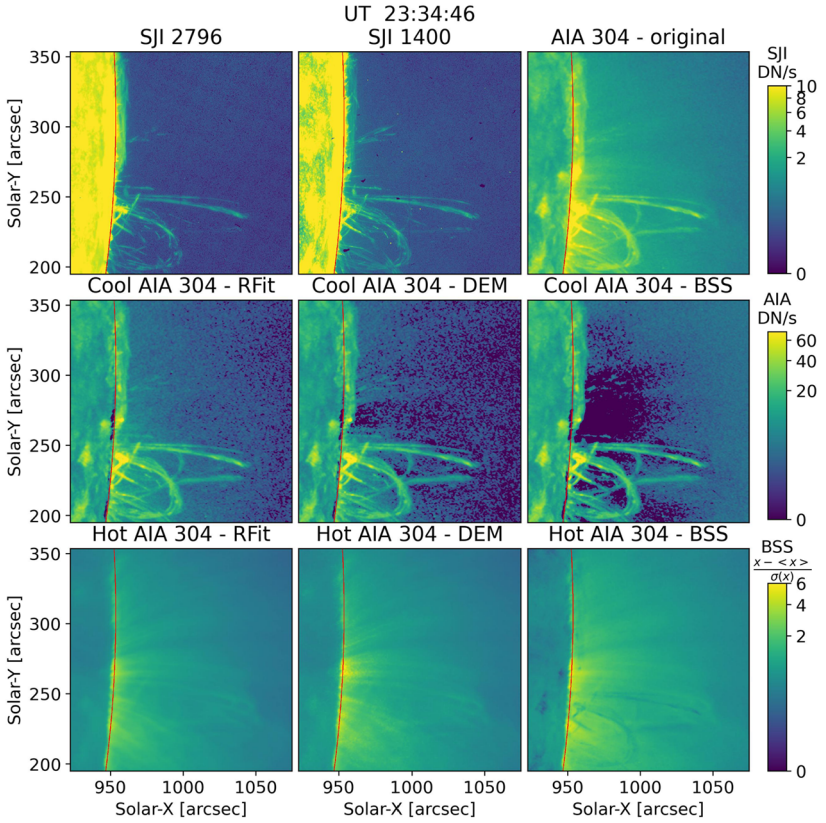

Figure 13 Co-observed FOV between IRIS and SDO for the quiescent stage. The top row shows the SJI 2796 Å (left) and 1400 Å (centre) passbands, and the original AIA 304 Å image (right). The middle row shows the cool AIA 304 Å component obtained with the RFit (left), DEM-based (centre) and BSS (right) methods. The bottom row shows the hot 304 Å versions with the different methods in the same order. Note that the intensity is on a logarithmic scale to better show the noise levels. Values of 0.5 and 1 have been added to the cool BSS and hot BSS images, respectively, to avoid most negative values. The region on the right-hand side of the red curve is the region used for the correlation analysis and rain-quantity calculation, shown in Figures 18 and 19.

(this cannot be done with BSS) to provide an idea of the real intensity values off-limb structures can have. To fully appreciate the gained contrast for the off-limb cool structures in the filtered images, we show in Figure 14 only the structures above noise levels, that is, with intensity values above a threshold of 0.18 DN s^{-1}, 0.3 DN s^{-1}, and 7 DN s^{-1} for the SJI 2796, SJI 1400 Å and cool AIA 304 Å (RFit and DEM) images, respectively. The noise threshold corresponds to values of -0.5 and -1 in the cool and hot BSS images, respectively, and we therefore add 0.5 and 1 (respectively) to the images prior to the logarithmic-scale plotting. These noise thresholds are estimated by averaging over a region on the top right corner of the image sequence, where none or little cool and hot structure is observed ($x > 1060''$ and $y > 340''$). Comparing the faint coronal rain off-limb we note, as expected, great similarity across the IRIS and cool AIA images. Almost every rain event in SJI 1400 Å or SJI 2796 Å appears in a cool 304 Å image. The RFit and DEM-based methods seem to capture even the faintest cool pixels better, while some of these are removed in the BSS image. As shown in

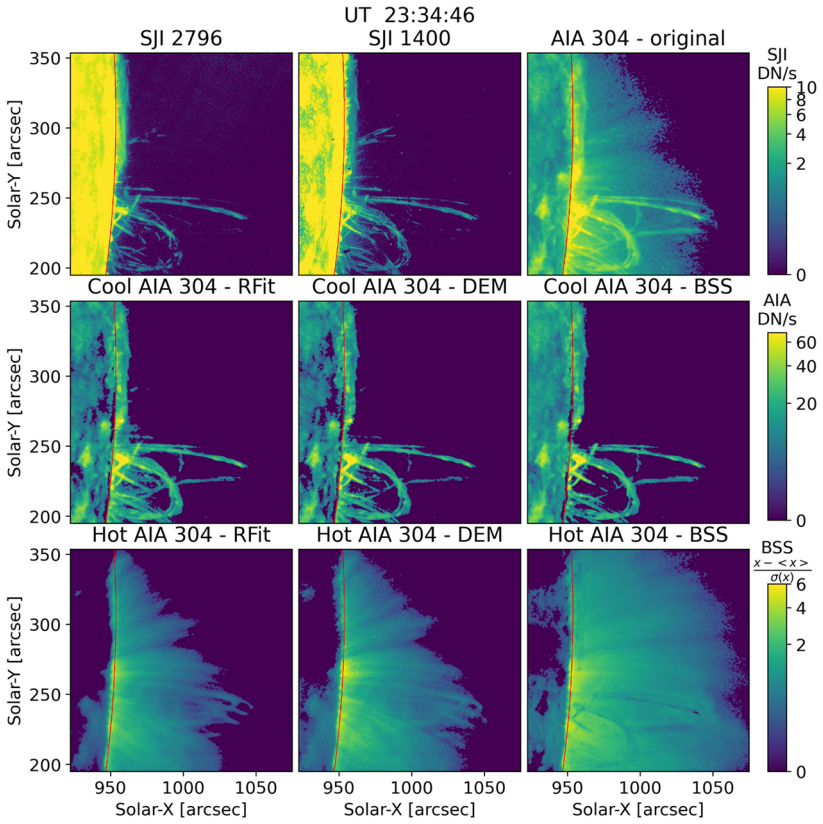

Figure 14 Same as in Figure 13 but setting the lower threshold intensity values above the noise (see text for details). See accompanying animation.

the previous section, the BSS method produces stronger inhomogeneity in the background, with larger temporal variation (see animation accompanying Figure 13). The hot 304 Å images are very similar during this quiescent stage, as already mentioned in the previous section.

In Figures 15, 16 and 17 we show, respectively, a time close to the intensity peak (UT 00:11:52), a time during the gradual phase immediately prior to coronal-rain appearance (UT 00:53:36) and a later time in the gradual phase with the flare-driven coronal rain (UT 01:14:37, corresponding to the same flaring time used in previous images). From the start of the flare and during the gradual phase prior to the appearance of the rain we note the appearance of a diffuse and faint region in the SJI 1400 Å image, also observed in the original 304 Å image, clearly seen in Figures 15 and 16 (see also animation of Figure 13). The temperature maps from the DEM in Figure 7 reveal very hot ($\approx$ 10 MK) plasma in this region. The emission in SJI 1400 Å can be understood by the 55 Å-wide wavelength range of this passband, which therefore also includes emission from the Fe XXI 1354.08 Å forming at $\approx 10^7$ K. This diffuse emission is not present in the SJI 2796, which further confirms a hot origin. At peak time, the hot 304 Å images reveal a flare loop at the same location of the diffuse 1400 Å emission, best seen in the hot RFit image, followed by the hot DEM image and barely in the hot BSS image. It is therefore highly likely that this hot emission is due to

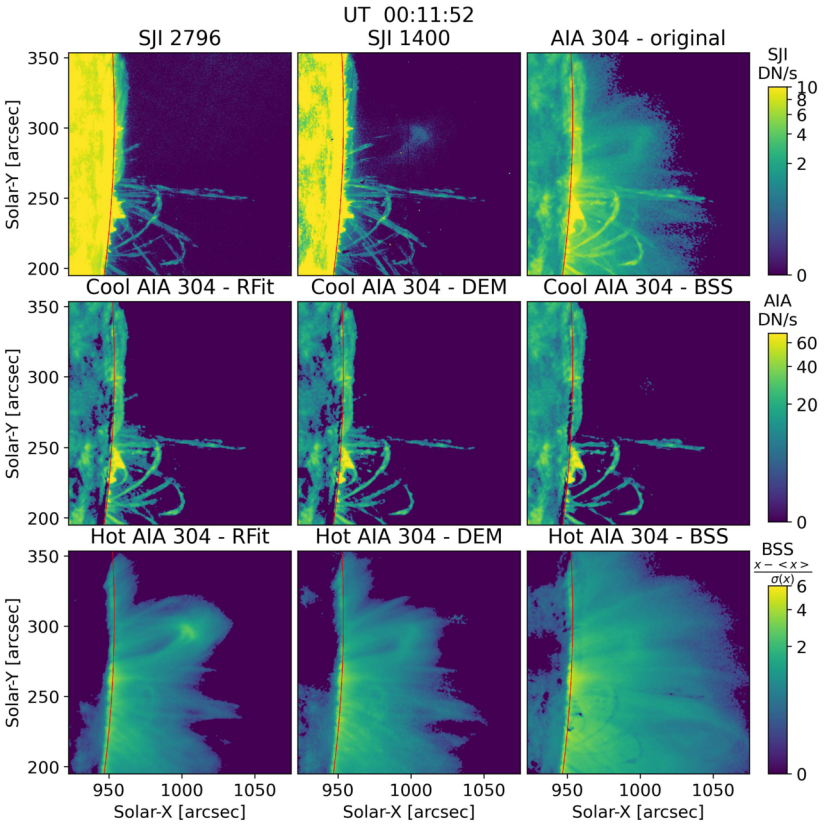

Figure 15 Same as in Figure 14 but close to the peak of the flare.

the contribution of Ca XVIII 302.19 Å, which forms at ≈ 10 MK (see Figure 2). At this stage, the cool 304 Å images successfully remove all the hot emission. In Figure 16, which shows the stage immediately prior to coronal-rain appearance, the diffuse 1400 Å emission has significantly decreased and is now barely visible. The hot 304 Å images still show a strongly emitting loop, slightly lower in height to the loop at peak flare time seen in Figure 17. The cool 304 Å images are only partially successful at removing this emission. As shown in the animation, this cool 304 Å emission starts to appear increasingly with time after the peak of the flare, which goes above the noise level 30 min and 55 min after the flare start, respectively, in the RFit and DEM images. The DEM images reveal rapid cooling during this time frame, with progressively stronger emission in the $\log T = 5.5$–5.6 temperature bin. Therefore, it is likely that the cool emission seen in the cool 304 Å images prior to the appearance of the rain corresponds to emission between $\log T = 5.1$ and $\log T = 5.5$, which is not removed by the RFit and DEM methods. On the other hand, the BSS images show emission roughly one minute prior to the appearance of the rain in SJI 1400 Å and is therefore the most successful at removing this warm emission. This probably reflects the distinct morphology of the rain at cool 10^4–10^5 K temperatures. However, hot emission can also be compact and be wrongly associated with the cool component. This effect is seen in Figure 17, where the hot BSS image has dark localised patches in the flare loop, which therefore appear brighter in the cool BSS images.

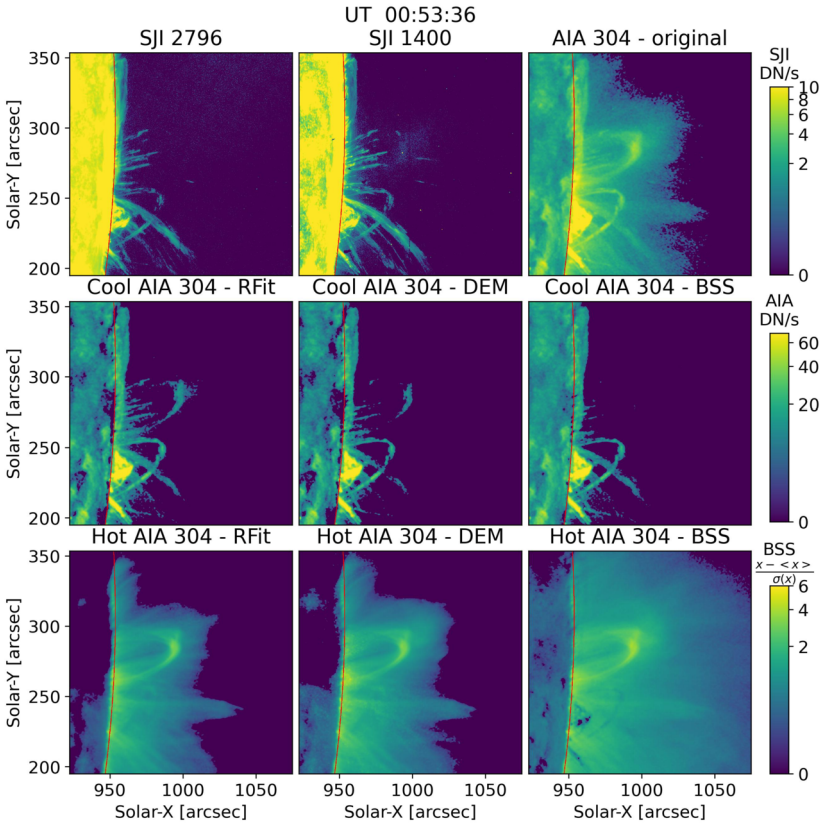

Figure 16 Same as in Figure 14 but for a time during the gradual phase and immediately prior to coronal-rain appearance.

In Figure 18 we calculate the Pearson correlation coefficient between each pair of IRIS (SJI 1400 Å or 2796) and each cool AIA 304 Å image obtained with all methods and for all the observational sequence. Since we are mainly interested in the cool structures off-limb, for this analysis we remove the on-disk portion of the images and the chromosphere such that most of the spicular region is masked (indicated by the red curve in Figure 13). Also, since the IRIS SJI instrument has ≈ 1.8 times higher spatial resolution, a Gaussian smoothing with a FWHM equal to this factor is applied to mimic the effect of the coarser point-spread function (PSF) from AIA. In the case of coronal rain, the lower spatial resolution leads to wider rain clumps (Şahin et al. 2023), so it is an important step prior to correlation. In order to avoid the effect of noise, in this calculation we only consider intensity values above a threshold of, respectively, 0.18 DN s^{-1}, 0.3 DN s^{-1} and 7 DN s^{-1} for the SJI 2796, SJI 1400 and AIA 304 Å images except those from BSS. For the cool BSS images we take a lower threshold of -0.5 (same as for Figure 14). Although no major cosmic-ray episodes occur (such as those caused by the passage of the satellite through the South Atlantic Anomaly), we also only consider pixels with values below 200 DN s^{-1} and 1000 DN s^{-1} for the SJI images and cool AIA 304 Å images, respectively. These upper thresholds are estimated based on cosmic-ray values for the current dataset, but also for limiting the influence of the very bright (flaring) structures and focus the correlation on the cool structures that are

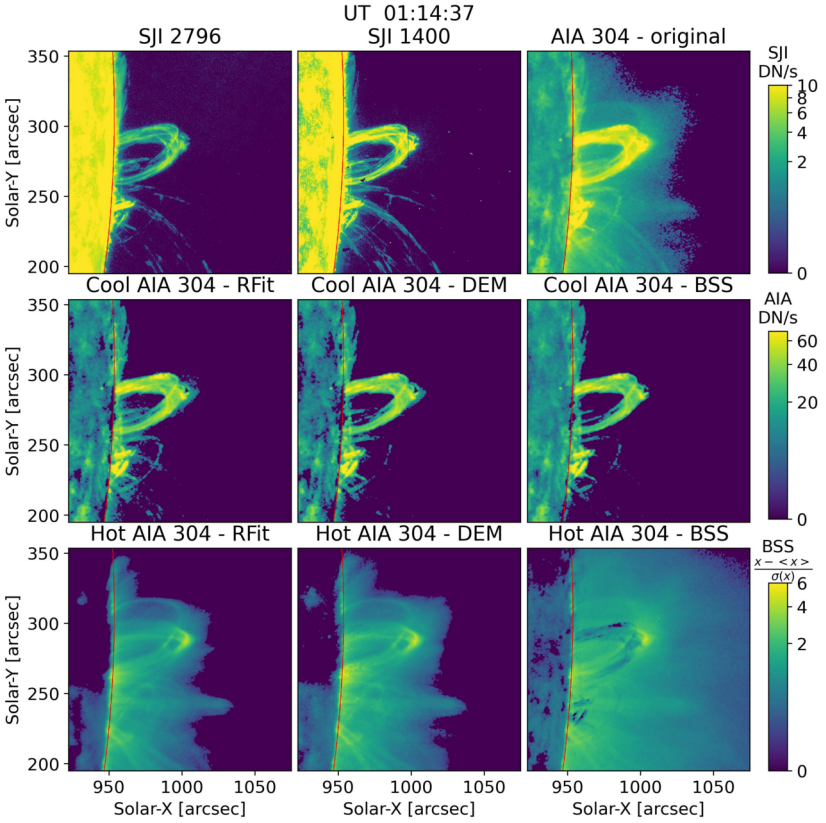

Figure 17 Same as in Figure 13 but for a time during the gradual phase with the flare-driven coronal rain (same flaring time as in the previous section).

much dimmer. Furthermore, in order to remove as much as possible the effect of opacity, we binarise the images and set to 1 all pixel values within the previous ranges, and to 0 all the remaining pixels. We obtain correlation values between the cool 304 Å images and either SJI passband between 0.6 and 0.9, while the corresponding values for the original 304 Å image oscillate around 0.5. We note a strong correlated evolution between the SJI-Cool 304 Å pair and the SJI-SJI pair, which reflects the success in the cool–hot 304 Å decomposition. The small decreases in the correlation are probably due to the appearance of the hot diffuse component in the SJI 1400 Å as seen around $t = 40$ min, and the emission between $\log T = 5.1$ and $\log T = 5.5$ for the cool 304 Å images, which happen at different times. Indeed, once the flare-driven rain appears at $t \approx 90$ min, all correlation curves strongly increase. This is further confirmed by the correlation with SJI 2796 Å, which does not include any hot emission, for which we see the highest correlation values (particularly with RFit and DEM). The largest variation is seen for the BSS method, probably due to the pre-whitening condition of the FastICA, which includes division by the standard deviation (and is thus subject to time variation). Among the methods, the RFit method seems to provide the best correlation with SJI 1400 Å (and SJI 2796), and very close to the correlation values obtained between the SJI passbands.

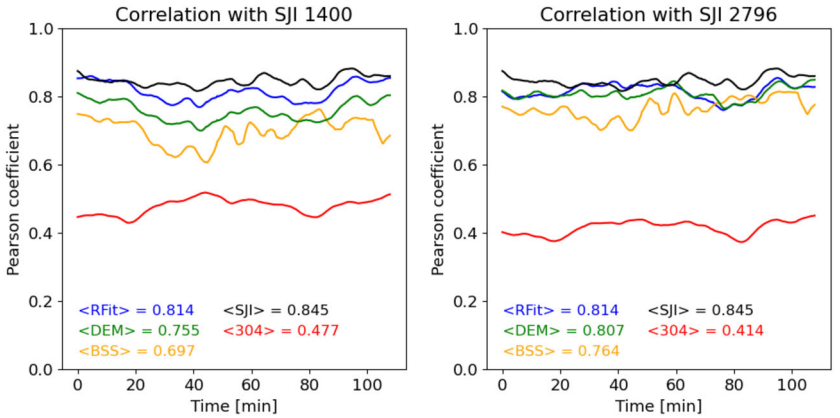

Figure 18 Pearson correlation coefficient for each IRIS (SJI 1400 Å on left panel, SJI 2796 Å on right panel) and Cool AIA 304 Å image pair in the observational sequence. The off-limb region corresponding to the portion above the red curve shown in Figures 13 to 17 is used for the correlation. Also, binarised images setting to 1 everything above a minimum and below a maximum intensity thresholds (and everything else to 0) are used to avoid effects from noise and cosmic rays. See text for further details. The average Pearson correlation coefficient over the entire sequence is shown at the bottom in the colour corresponding to the respective pair. The '<SJI>' symbol denotes correlation between the two SJI passbands.

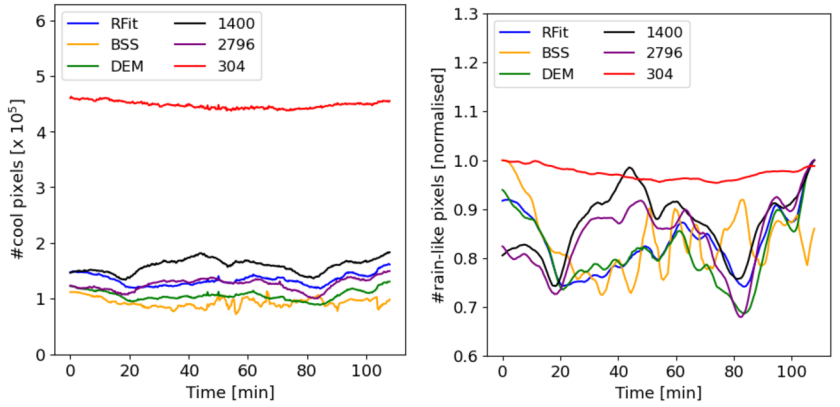

Figure 19 (Left) Number of cool pixels over time for each passband (shown in legend). A cool pixel is defined as being above a specific height and intensity threshold (see text for further details). (Right) Normalised cool pixel number over time. A smoothing over 9 min has been applied to all curves for the right panel.

We further calculate the number of cool pixels for each snapshot in each passband for the same off-limb region as for the Pearson correlation calculation (above the red curve shown in Figure 13. The intensity thresholds are the same as those taken for the correlation calculation (we also take the upper threshold in the intensity mentioned above to avoid very high flaring intensities or cosmic rays). While a significant portion of the captured cool material corresponds to coronal rain, we also capture the low-lying prominence (visible at $x > 300''$ and $y \approx 950''$), tips of spicules and other cool transient structures. Therefore, we simply refer to these pixels as cool pixels. In Figure 19 (left panel) we show the total number of cool pixels over time for the SJI 1400, the original AIA 304 Å and cool AIA 304 Å

images. We can see that the original 304 Å image shows almost an order of magnitude more pixels that would be incorrectly defined as cool pixels according to the definition above. On the other hand, all three methods give a similar number of cool pixels for each snapshot (within a factor of two). The BSS method shows the lowest number and relatively large variation. As for the Pearson correlation, we expect this to be due to the pre-whitening process prior to the application of FastICA. For better comparison across the methods we normalise each curve by its maximum and show in the right panel of Figure 19 the variation over time. Furthermore, we apply a smoothing with a window size of ≈ 9 min to compare the trends rather than the high-frequency variations produced by the methods (such as BSS). We note a similar variation across the methods, with RFit and DEM very similar to each other, and with no method perfectly matching all the ups and downs seen in SJI 1400 Å. However, the RFit and BSS methods provide the best and worst results to 1400 Å and 2796, respectively (in terms of proximity to the curves). The 1400 Å curve displays a maximum around $t = 40$ min, which is noticeably absent from the curves corresponding to the cool 304 Å images. This peak is due to the appearance of the hot flaring loop, seen in Fe XXI emission as previously discussed, and is also responsible for the minimum in the correlation at the same time between SJI 1400Å and the cool 304 Å images in Figure 18.

5. Discussion and Conclusions

In this paper, we have presented three methods that allow us to separate cool and hot components present in the AIA 304 Å passband, forming at $\approx 10^5$ K and $\approx 10^{6.2}$ K, respectively. The motivation behind this is to better identify the cool and hot structures in the corona, and characterise their evolution over time. This is a general problem in solar physics, particularly relevant to coronal heating. Advancing on the coronal heating problem implies to first properly identify the heating that occurs in the solar atmosphere, and carefully assess how hot the plasma can become. Counter-intuitively, a result of coronal heating is the presence of large amounts of cool material in the corona in the form of prominences and coronal rain (Antolin and Froment 2022). Properly quantifying this cool coronal plasma is therefore important but constitutes a major challenge due to the small size and faint intensities of the cool material. Disambiguation between hot and cool plasma emission has been a recurrent problem (Del Zanna and Mason 2018). For example, the AIA 94 emission is often considered as evidence for hot emission from Fe XVIII at 7 MK, but the presence of warm emission from various Fe ions within the passband demands caution (Aschwanden and Boerner 2011; Testa et al. 2012; Del Zanna 2013).

Observations in the AIA 304 Å passband constitute by far the largest data pool for detecting cool material around 10^5 K temperatures at coronal heights given the full FOV, cadence and lifetime of AIA. The emission in the 304 Å passband from the cool material in the corona is minimal compared to the transition-region background for on-disc observations, so the detection is largely limited to the off-limb corona. However, observations off-limb suffer from significant LOS superposition, meaning that the hot emission in the 304 Å passband (for which the response function is at least an order of magnitude lower than the cool component) ends up having intensities of the same order of magnitude as the cool emission.

The three proposed methods for decomposing the cool and hot emission are based on the AIA response functions ('RFit'), the Differential Emission Measure ('DEM') technique and the Blind Source Separation ('BSS') technique. The RFit and DEM methods mainly rely on the different temperatures of plasma emission, while the BSS mainly relies on the different morphology of the structure. Due to the usually different morphology between the

cool and hot plasma (with the chromospheric material such as rain and prominences being clumpy rather than diffuse as for the hot emission, due to the differences in localisation of the emission along the LOS), the BSS method has an indirect reliance on temperature. The RFit method works by linearly fitting the hot component in the 304 Å response function with the other EUV response functions. The DEM-based method provides the amount of emission measured in the hot (optically thin) temperature range that is sensitive to the 304 Å passband, and therefore relies on the accuracy of the DEM algorithm. The BSS method morphologically separates the image in different source functions, thereby leading to more thermally pure components indirectly. By construction, given an AIA 304 Å image, all three methods allow us to obtain two different versions of the same image, with a version that contains solely the cool or hot components.

The RFit and DEM methods heavily rely on the AIA response functions sensitivity and the inter-channel calibration, which vary over time due to instrumental degradation. Hence, it is likely that these methods will perform worse at later stages in the AIA lifetime. On the other hand, since the BSS method only relies on the morphological differences across channels rather than the intensity differences linked to temperature, the BSS method may perform better over time.

We have compared each method selecting a dataset in 2014 with an AR off-limb, and focusing on the off-limb region that presents quiescent and flaring corona at different times. The variety in the observed energy release and atmospheric response to heating provides a further test for robustness for each method. To quantify the results we have used data from IRIS/SJI 1400 Å and 2796 Å passbands, which correctly point to the presence of chromospheric and (lower) transition-region material.

We have seen that each method presents pros and cons that we summarise as follows:

- All three methods give satisfactory results in the hot and cool decomposition within a 304 Å image, particularly during quiescent coronal stages. The gained contrast over the background is similar to that of IRIS, with 100 – 200% gain compared to the original image. The RFit and DEM methods give similar results, temporally consistent (low variability) and highly correlated with the cool emission observed with IRIS (particularly in the SJI 2796 Å channel). On the other hand, the BSS method is less accurate and more variable over time.
- The hot emission during the flare peak is best recovered by the RFit (first), the DEM (second) and BSS (third) methods.
- The RFit and DEM methods fail at fully removing the emission during the catastrophic cooling of the gradual flare phase and prior to the rain appearance. However, it is likely that this emission originates in the $\log T = 5.1 - 5.5$ temperature range, which cannot be accounted for by construction of the methods. On the other hand, the BSS method successfully removes all such 'warm' emission until the appearance of the cool rain.
- All methods identify a hot thin layer at the footpoints of the active-region loops, and also some on-disc hot emission in quiet-Sun regions.
- Our hot–cool decomposition analysis suggests significant very hot plasma emission during flare times at ≈ 10 MK from Ca XVIII 302.19 Å, and Fe XXI 1354.08 Å within the 304 Å and 1400 Å passbands, respectively.
- A caveat of the BSS method is that it can wrongly attribute hot and highly localised flare emission as cool. Furthermore, the required pre-whitening of images introduces large temporal variation and impedes recovery of the physical (intensity) units in the resulting decomposition.

- The RFit method is the fastest of all three, computing 600 images in less than 3 s in a standard computer. On the other hand, the BSS method requires about 1 – 2 orders of magnitude larger times.

In general, the proposed methods are successful at identifying the cool emission within the 304 Å passband, thereby allowing us to better detect cool material off-limb such as coronal rain, prominence eruptions or spicules in the 304 Å passband. In Şahin et al. (2023) the BSS method was applied to improve coronal-rain detection in the 304 Å passband. However, we identify the RFit method as the best performing method for the cool and hot disambiguation. Another major advantage of this method over the DEM and BSS methods is that it completely bypasses computationally expensive calculations such as DEM and FastICA. These methods can be applied whenever there is good temperature coverage, particularly around the region of hot emission with the 304 Å passband (with major contributor the Si XI emission at 303.32 Å for the AIA 304 Å passband, forming at ≈ 1.5 MK), so in principle they can be also applicable to other current and future observatories that have similar 304 Å passbands and high-temperature coverage such as STEREO, PROBA 2 and MUSE. The same techniques may also be applied to separate the cool and hot emissions, or hot and flaring emissions in other AIA channels, such as AIA 94 (Del Zanna 2013) and are also applicable from one instrument to another. A potential application of the methods would be to separate the hot emission from Fe XXI from the cool emission in the SJI 1330 and 1400 Å passbands of IRIS. This is the subject of future work.

Acknowledgments P.A. would like to thank M. Cheung and B. De Pontieu for fruitful discussions that contributed to this work. We would also like to thank the anonymous reviewer whose very insightful comments and detailed revision have significantly improved this work. Data are courtesy of SDO and IRIS. SDO is a mission for NASA's Living With a Star (LWS) program. IRIS is a NASA small explorer mission developed and operated by LMSAL with mission operations executed at NASA Ames Research Center and major contributions to downlink communications funded by ESA and the Norwegian Space Centre. This research was supported by the International Space Science Institute (ISSI) in Bern, through ISSI International Team project #545 ('Observe Local Think Global: What Solar Observations can Teach us about Multiphase Plasmas across Physical Scales'). All images in this manuscript have been made with Matplotlib on Python (Hunter 2007). This research used version 4.1.5 (Mumford et al. 2023) of the SunPy open-source software package (The SunPy Community et al. 2020). The AIA response functions have been computed with SSW/IDL (Freeland and Handy 1998).

Author contributions P.A. produced most figures and wrote the main manuscript text. F.A. produced Figure 1 and reviewed the manuscript. E.W. contributed to the python script for the data analysis. E.S. contributed to the python script for the data analysis and reviewed manuscript. R.O. reviewed the manuscript.

Funding P.A. acknowledges funding from the STFC Ernest Rutherford Fellowship (No. ST/R004285/2). This publication is part of the R+D+i project PID2020-112791GB-I00, financed by MCIN/AEI/10.13039/501100011033.

Data Availability No datasets were generated or analysed during the current study. The methods presented in this article can be accessed in this GitHub page and also available at Antolin (2024).

Declarations

Competing interests The authors declare no competing interests.

References

Andretta, V., Del Zanna, G., Jordan, S.D.: 2003, The EUV helium spectrum in the quiet Sun: a by-product of coronal emission? *Astron. Astrophys.* **400**, 737. DOI. ADS.

Antolin, P.: 2020, Thermal instability and non-equilibrium in solar coronal loops: from coronal rain to long-period intensity pulsations. *Plasma Phys. Control. Fusion* **62**, 014016. DOI. ADS.

Antolin, P.: 2024, Cool304: Decomposing the AIA 304 channel into its cool and hot components, Zenodo. DOI.

Antolin, P., Froment, C.: 2022, Multi-scale variability of coronal loops set by thermal non-equilibrium and instability as a probe for coronal heating. *Front. Astron. Space Sci.* **9**. DOI.

Antolin, P., Shibata, K., Vissers, G.: 2010, Coronal rain as a marker for coronal heating mechanisms. *Astrophys. J.* **716**, 154. DOI. ADS.

Antolin, P., Vissers, G., Pereira, T.M.D., Rouppe van der Voort, L., Scullion, E.: 2015, The multithermal and multi-stranded nature of coronal rain. *Astrophys. J.* **806**, 81. DOI. ADS.

Aschwanden, M.J., Boerner, P.: 2011, Solar corona loop studies with the atmospheric imaging assembly. I. Cross-sectional temperature structure. *Astrophys. J.* **732**, 81. DOI.

Cheng, C.-C., Smith, J.B., Tandberg-Hanssen, E.: 1980, Morphology and spatial distribution of XUV and X-ray emissions in an active region observed from SKYLAB. *Solar Phys.* **67**, 259. DOI. ADS.

Cheung, M.C.M., Boerner, P., Schrijver, C.J., Testa, P., Chen, F., Peter, H., Malanushenko, A.: 2015, Thermal diagnostics with the atmospheric imaging assembly on board the solar dynamics observatory: a validated method for differential emission measure inversions. *Astrophys. J.* **807**, 143. DOI. ADS.

Cheung, M.C.M., Rempel, M., Chintzoglou, G., Chen, F., Testa, P., Martínez-Sykora, J., Sainz Dalda, A., DeRosa, M.L., Malanushenko, A., Hansteen, V., De Pontieu, B., Carlsson, M., Gudiksen, B., McIntosh, S.W.: 2019, A comprehensive three-dimensional radiative magnetohydrodynamic simulation of a solar flare. *Nat. Astron.* **3**, 160. DOI.

Common, P., Jutten, C.: 2010, *Handbook of Blind Source Separation: Independent Component Analysis and Blind Deconvolution*, Academic Press, Oxford.

De Pontieu, B., Title, A.M., Lemen, J.R., Kushner, G.D., Akin, D.J., Allard, B., Berger, T., Boerner, P., Cheung, M., Chou, C., Drake, J.F., Duncan, D.W., Freeland, S., Heyman, G.F., Hoffman, C., Hurlburt, N.E., Lindgren, R.W., Mathur, D., Rehse, R., Sabolish, D., Seguin, R., Schrijver, C.J., Tarbell, T.D., Wülser, J.-P., Wolfson, C.J., Yanari, C., Mudge, J., Nguyen-Phuc, N., Timmons, R., van Bezooijen, R., Weingrod, I., Brookner, R., Butcher, G., Dougherty, B., Eder, J., Knagenhjelm, V., Larsen, S., Mansir, D., Phan, L., Boyle, P., Cheimets, P.N., DeLuca, E.E., Golub, L., Gates, R., Hertz, E., McKillop, S., Park, S., Perry, T., Podgorski, W.A., Reeves, K., Saar, S., Testa, P., Tian, H., Weber, M., Dunn, C., Eccles, S., Jaeggli, S.A., Kankelborg, C.C., Mashburn, K., Pust, N., Springer, L., Carvalho, R., Kleint, L., Marmie, J., Mazmanian, E., Pereira, T.M.D., Sawyer, S., Strong, J., Worden, S.P., Carlsson, M., Hansteen, V.H., Leenaarts, J., Wiesmann, M., Aloise, J., Chu, K.-C., Bush, R.I., Scherrer, P.H., Brekke, P., Martinez-Sykora, J., Lites, B.W., McIntosh, S.W., Uitenbroek, H., Okamoto, T.J., Gummin, M.A., Auker, G., Jerram, P., Pool, P., Waltham, N.: 2014, The interface region imaging spectrograph (IRIS). *Solar Phys.* **289**, 2733. DOI. ADS.

Del Zanna, G.: 2013, The multi-thermal emission in solar active regions. *Astron. Astrophys.* **558**, A73. DOI. ADS.

Del Zanna, G., Mason, H.E.: 2018, Solar UV and X-ray spectral diagnostics. *Living Rev. Solar Phys.* **15**, 5. DOI. ADS.

Del Zanna, G., Dere, K.P., Young, P.R., Landi, E.: 2021, CHIANTI—an atomic database for emission lines. XVI. Version 10, further extensions. *Astrophys. J.* **909**, 38. DOI. ADS.

Delabrouille, J., Cardoso, J.-F., Patanchon, G.: 2003, Multidetector multicomponent spectral matching and applications for cosmic microwave background data analysis. *Mon. Not. Roy. Astron. Soc.* **346**, 1089. DOI.

Dere, K.P., Landi, E., Mason, H.E., Monsignori Fossi, B.C., Young, P.R.: 1997, CHIANTI - an atomic database for emission lines. *Astron. Astrophys. Suppl. Ser.* **125**, 149. DOI. ADS.

Dudok de Wit, T., Auchère, F.: 2007, Multispectral analysis of solar EUV images: linking temperature to morphology. *Astron. Astrophys.* **466**, 347. DOI.

Dudok de Wit, T., Moussaoui, S., Guennou, C., Auchère, F., Cessateur, G., Kretzschmar, M., Vieira, L.A., Goryaev, F.F.: 2013, Coronal temperature maps from solar EUV images: a blind source separation approach. *Solar Phys.* **283**, 31. DOI.

Feldman, U., Widing, K.G., Warren, H.P.: 1999, Morphology of the quiet solar upper atmosphere in the $4\times10^4 < T_e < 1.4\times10^6$ K temperature regime. *Astrophys. J.* **522**, 1133. DOI. ADS.

Freeland, S.L., Handy, B.N.: 1998, Data analysis with the SolarSoft system. *Solar Phys.* **182**, 497. DOI. ADS.

Gallagher, P.T., Phillips, K.J.H., Harra-Murnion, L.K., Keenan, F.P.: 1998, Properties of the quiet Sun EUV network. *Astron. Astrophys.* **335**, 733. ADS.

Golding, T.P., Leenaarts, J., Carlsson, M.: 2017, Formation of the helium extreme-UV resonance lines. *Astron. Astrophys.* **597**, A102. DOI.

Guennou, C., Auchère, F., Soubrié, E., Bocchialini, K., Parenti, S., Barbey, N.: 2012, On the accuracy of the differential emission measure diagnostics of solar plasmas. Application to SDO/AIA. I. Isothermal plasmas. *Astrophys. J. Suppl.* **203**, 25. DOI. ADS.

Hannah, I.G., Kontar, E.P.: 2012, Differential emission measures from the regularized inversion of Hinode and SDO data. *Astron. Astrophys.* **539**, A146. DOI. ADS.

Hinode Review Team, Al-Janabi, K., Antolin, P., Baker, D., Bellot Rubio, L.R., Bradley, L., Brooks, D.H., Centeno, R., Culhane, J.L., Del Zanna, G., Doschek, G.A., Fletcher, L., Hara, H., Harra, L.K., Hillier, A.S., Imada, S., Klimchuk, J.A., Mariska, J.T., Pereira, T.M.D., Reeves, K.K., Sakao, T., Sakurai, T., Shimizu, T., Shimojo, M., Shiota, D., Solanki, S.K., Sterling, A.C., Su, Y., Suematsu, Y., Tarbell, T.D., Tiwari, S.K., Toriumi, S., Ugarte-Urra, I., Warren, H.P., Watanabe, T., Young, P.R.: 2019, Achievements of Hinode in the first eleven years. *Publ. Astron. Soc. Japan* **71**, R1. DOI.

Hunter, J.D.: 2007, Matplotlib: a 2D graphics environment. *Comput. Sci. Eng.* **9**, 90. DOI.

Hyvarinen, A.: 1999, Fast and robust fixed-point algorithms for independent component analysis. *IEEE Trans. Neural Netw.* **10**, 626. DOI.

Hyvärinen, A., Oja, E.: 2000, Independent component analysis: algorithms and applications. *Neural Netw.* **13**, 411. DOI. https://www.sciencedirect.com/science/article/pii/S0893608000000265.

Ishikawa, S., Glesener, L., Krucker, S., Christe, S., Buitrago-Casas, J., Narukage, N., Vievering, J.: 2017, Detection of nanoflare-heated plasma in the solar corona by the FOXSI-2 sounding rocket. *Nat. Astron.* **1**, 771. DOI.

Jefferies, J.T., Orrall, F.Q., Zirker, J.B.: 1972, The interpretation of total line intensities from optically thin gases. I: a general method. *Solar Phys.* **22**, 307. DOI. ADS.

Jordan, C.: 1976, The structure and energy balance of solar active regions. *Phil. Trans. Roy. Soc. London A* **281**, 391. DOI. ADS.

Jordan, C.: 1980, Helium line emission: its relation to atmospheric structure. *Phil. Trans. Roy. Soc. London A* **297**, 541. DOI. ADS.

Kashyap, V., Drake, J.J.: 1998, Markov-chain Monte Carlo reconstruction of emission measure distributions: application to solar extreme-ultraviolet spectra. *Astrophys. J.* **503**, 450. DOI. ADS.

Kuruoglu, E.E.: 2010, Bayesian source separation for cosmology. *IEEE Signal Process. Mag.* **27**, 43. DOI.

Landi, E., Del Zanna, G., Young, P.R., Dere, K.P., Mason, H.E.: 2012, CHIANTI - an atomic database for emission lines. XII. Version 7 of the database. *Astrophys. J.* **744**, 99. DOI. ADS.

Leenaarts, J., Pereira, T.M.D., Carlsson, M., Uitenbroek, H., De Pontieu, B.: 2013, The formation of IRIS diagnostics. I. A quintessential model atom of Mg II and general formation properties of the Mg II h&k lines. *Astrophys. J.* **772**, 89. DOI. ADS.

Lemen, J.R., Title, A.M., Akin, D.J., Boerner, P.F., Chou, C., Drake, J.F., Duncan, D.W., Edwards, C.G., Friedlaender, F.M., Heyman, G.F., Hurlburt, N.E., Katz, N.L., Kushner, G.D., Levay, M., Lindgren, R.W., Mathur, D.P., McFeaters, E.L., Mitchell, S., Rehse, R.A., Schrijver, C.J., Springer, L.A., Stern, R.A., Tarbell, T.D., Wuelser, J.-P., Wolfson, C.J., Yanari, C., Bookbinder, J.A., Cheimets, P.N., Caldwell, D., Deluca, E.E., Gates, R., Golub, L., Park, S., Podgorski, W.A., Bush, R.I., Scherrer, P.H., Gummin, M.A., Smith, P., Auker, G., Jerram, P., Pool, P., Soufli, R., Windt, D.L., Beardsley, S., Clapp, M., Lang, J., Waltham, N.: 2012, The atmospheric imaging assembly (AIA) on the solar dynamics observatory (SDO). *Solar Phys.* **275**, 17. DOI. ADS.

Loboda, I., Reva, A., Bogachev, S., Kirichenko, A., Ulyanov, A.: 2023, Separating He II and Si XI emission components in off-limb 304 Å observations. *Solar Phys.* **298**, 136. DOI. ADS.

Moussaoui, S., Brie, D., Mohammad-Djafari, A., Carteret, C.: 2006, Separation of non-negative mixture of non-negative sources using a Bayesian approach and MCMC sampling. *IEEE Trans. Signal Process.* **54**, 4133. DOI.

Mumford, S.J., Freij, N., Stansby, D., Christe, S., Ireland, J., Mayer, F., Shih, A.Y., Hughitt, V.K., Ryan, D.F., Liedtke, S., Hayes, L., Pérez-Suárez, D., I., V.K., Barnes, W., Chakraborty, P., Inglis, A., Pattnaik, P., Sipőcz, B., MacBride, C., Sharma, R., Leonard, A., Hewett, R., Hamilton, A., Manhas, A., Panda, A., Earnshaw, M., Choudhary, N., Kumar, A., Singh, R., Chanda, P., Haque, M.A., Kirk, M.S., Mueller, M., Konge, S., Srivastava, R., Wentzel-Long, M., Jain, Y., Bennett, S., Baruah, A., Arbolante, Q., Charlton, M., Maloney, S., Mishra, S., Paul, J.A., Verma, A., Chorley, N., Chouhan, A., Himanshu, Mason, J.P., Zivadinovic, L., Modi, S., Sharma, Y., Naman9639, Bobra, M.G., Rozo, J.I.C., Manley, L., Ivashkiv,

K., Laitinen, T., Chatterjee, A., von Forstner, J.F., Bazán, J., Stern, K.A., Gieseler, J., Evans, J., Jain, S., Malocha, M., Ghosh, S., Airmansmith97, Stańczak, D., Singh, R.R., Visscher, R.D., Verma, S., SophieLemos, Agrawal, A., Alam, A., Buddhika, D., Pathak, H., Rideout, J.R., Sharma, S., Park, J., Bates, M., Wilson, A., Shukla, D., Giger, M., Mishra, P., Sharma, D., Goel, D., Taylor, G., Cetusic, G., Reiter, G., Jacob, Inchaurrandieta, M., Dacie, S., Dubey, S., Eigenbrot, A., Bray, E.M., Surve, R., Zahniy, S., Sidhu, S., Meszaros, T., Parkhi, U., Russell, W., Bose, A., Pandey, A., Price-Whelan, A., J, A., Chicrala, A., Ankit, Guennou, C., D'Avella, D., Williams, D., Verma, D., Ballew, J., Agrawal, K., Murphy, N., Lodha, P., Robitaille, T., Augspurger, T., Krishan, Y., honey, neerajkulk, Bhope, A., Gaba, A.S., Hill, A., Mampaey, B., Wiedemann, B.M., Molina, C., Briseno, D.G., Keşkek, D., Habib, I., Letts, J., Singaravelan, K., Ranjan, K., Altunian, N., Streicher, O., Gomillion, R., Agarwal, S., Kothari, Y., Nomiya, Y., mridulpandey, Stevens, A.L., B, A., Bahuleyan, A., Kaszynski, A., W, A., Mehrotra, A., Tang, A., Sinha, A., Smith, A., Kustov, A., Stone, B., Bard, C., Arias, E., Tollerud, E., Dover, F.M., Verstringe, F., Kumar, G., Mathur, H., Babuschkin, I., Calixto, J., Wimbish, J., Qing, J., Buitrago-Casas, J.C., Krishna, K., Chaudhari, K., Hiware, K., Ghosh, K., Lyes, M.M., Mangaonkar, M., Cheung, M., Mendero, M., Dedhia, M., Schoentgen, M., Shahdadpuri, N., Srinivasan, N., Gyenge, N.G., Mekala, R.R., Das, R., Mishra, R., Sharma, R., Srikanth, S., Jain, S., Kannojia, S., Yadav, T., Paul, T., Wilkinson, T.D., Caswell, T.A., Braccia, T., Pereira, T.M.D., Gates, T., Dang, T.K., Bankar, V., Jamieson, W., Agrawal, Y., platipo, resakra, tal66, yasintoda, Attie, R., Murray, S.A.: 2023, SunPy, Zenodo. DOI.

Nuzillard, D., Bijaoui, A.: 2000, Blind source separation and analysis of multispectral astronomical images. *Astron. Astrophys. Suppl. Ser.* **147**, 129. DOI.

O'Dwyer, B., Del Zanna, G., Mason, H.E., Weber, M.A., Tripathi, D.: 2010, SDO/AIA response to coronal hole, quiet Sun, active region, and flare plasma. *Astron. Astrophys.* **521**, A21. DOI. ADS.

Olluri, K., Gudiksen, B.V., Hansteen, V.H., De Pontieu, B.: 2015, Synthesized spectra of optically thin emission lines. *Astrophys. J.* **802**, 5. DOI. ADS.

Pesnell, W.D., Thompson, B.J., Chamberlin, P.C.: 2012, The solar dynamics observatory (SDO). *Solar Phys.* **275**, 3. DOI. ADS.

Plowman, J., Caspi, A.: 2020, A fast, simple, robust algorithm for coronal temperature reconstruction. *Astrophys. J.* **905**, 17. DOI. ADS.

Reale, F.: 2010, Coronal loops: observations and modeling of confined plasma. *Living Rev. Solar Phys.* **7**, 5. ADS.

Rouppe van der Voort, L., De Pontieu, B., Pereira, T.M.D., Carlsson, M., Hansteen, V.: 2015, Heating signatures in the disk counterparts of solar spicules in interface region imaging spectrograph observations. *Astrophys. J. Lett.* **799**, L3. DOI. ADS.

Şahin, S., Antolin, P.: 2022, Prevalence of thermal nonequilibrium over an active region. *Astrophys. J. Lett.* **931**, L27. DOI. ADS.

Şahin, S., Antolin, P., Froment, C., Schad, T.A.: 2023, Spatial and temporal analysis of quiescent coronal rain over an active region. *Astrophys. J.* **950**, 171. DOI. ADS.

Testa, P., Pontieu, B.D., Martínez-Sykora, J., Hansteen, V., Carlsson, M.: 2012, Investigating the reliability of coronal emission measure distribution diagnostics using three-dimensional radiative magnetohydrodynamic simulations. *Astrophys. J.* **758**, 54. DOI.

The SunPy Community, Barnes, W.T., Bobra, M.G., Christe, S.D., Freij, N., Hayes, L.A., Ireland, J., Mumford, S., Perez-Suarez, D., Ryan, D.F., Shih, A.Y., Chanda, P., Glogowski, K., Hewett, R., Hughitt, V.K., Hill, A., Hiware, K., Inglis, A., Kirk, M.S.F., Konge, S., Mason, J.P., Maloney, S.A., Murray, S.A., Panda, A., Park, J., Pereira, T.M.D., Reardon, K., Savage, S., Sipőcz, B.M., Stansby, D., Jain, Y., Taylor, G., Yadav, T., Rajul, D.T.K.: 2020, The SunPy project: open source development and status of the version 1.0 core package. *Astrophys. J.* **890**. DOI.

Thompson, W.T., Brekke, P.: 2000, EUV full-Sun imaged spectral atlas using the SOHO coronal diagnostic spectrometer. *Solar Phys.* **195**, 45. DOI. ADS.

Tousey, R., Austin, W.E., Purcell, J.D., Widing, K.G.: 1965, The extreme ultraviolet emission from the Sun between the Lyman-alpha lines of H I and C VI. *Ann. Astrophys.* **28**, 755. ADS.

Vernazza, J.E., Reeves, E.M.: 1978, Extreme ultraviolet composite spectra of representative solar features. *Astrophys. J. Suppl.* **37**, 485. DOI. ADS.

Warren, H.P., Winebarger, A.R., Brooks, D.H.: 2012, A systematic survey of high-temperature emission in solar active regions. *Astrophys. J.* **759**, 141. DOI. ADS.

Wright, P.J., Cheung, M.C.M., Thomas, R., Galvez, R., Szenicer, A., Jin, M., Muñoz-Jaramillo, A., Fouhey, D.: 2019, DeepEM: demonstrating a deep learning approach to DEM inversion. Zenodo. DOI.

Zirin, H.: 1988, *Astrophysics of the Sun*, Cambridge University Press, Cambridge. ADS.